博士論文

Theoretical Study on Spatial Symmetry Breaking in Nonadiabatic Dynamics in Excited States

(空間対称性の破れを伴う励起状態非断熱動力学の理論的研究)

李 中偉

Li Zhong-wei

Abstract

Symmetry allowed conical intersection plays a central role in excited state symmetry-forbidden reactions. As an illustrative example as such, we track the dynamical sequence of spatial-symmetry breaking of B_4 cluster, which has a rich electronic structure in the low-lying excited states, to see how the relevant reaction proceeds. The semiclassical Ehrenfest method is used to detect the nonadiabatic electronic state mixing along the reactions. The essential feature of the nonadiabatic electron dynamics is clarified in terms of electron flux and unpaired-electron distribution induced by the nonadiabatic transitions. To facilitate understanding electron dynamics of symmetry breaking, we begin with symmetry consideration in terms of the Hückel orbitals, which are shown to be qualitatively useful enough to foresee the possible existence of symmetry allowed conical intersections.

Contents

1 General Introduction **1**

2 Choose B_4 as Case Study **7**

2.1 Introduction 7

2.2 A Symmetry Consideration in Terms of the Hückel Theory 9

2.2.1 Basic Bond Matrices 9

2.2.2 Description of *sp* Hybridization in the Hückel framework 11

2.2.3 Hückel Molecular Orbitals As the Bases of Irreducible Representations 13

2.2.4 Symmetry-allowed Conical Intersections Foreseen with the Hückel Theory . . 16

3 Theoretical Methods and Implementation **20**

3.1 Theoretical Background 20

3.1.1 Nonadiabatic Electronic Dynamics 20

3.1.2 Nonadiabatic Nuclear Dynamics 21

3.1.3 Electron Flux Analysis 22

3.1.4 Unpaired Electron Population Analysis 23

3.2 Integrals Calculating of Coupling Term 24

3.2.1 Prepare One-electron Coupling Constants a_{ij}^{IJ} 24

3.2.2 Prepare the Skeleton Integral S_{ij}^{kR} 25

3.2.3 Prepare U Matrix U_{ij}^{k} 26

3.3 Unique-Continuity of Molecular Orbitals 27

3.3.1 Theoretical Method 27

3.3.2 Numerical Illustration 28

4 Symmetry Breaking Dynamics of the Low-lying Excited States of B_4 **32**

4.1 Ground State: ^1A_g 33

4.1.1 SCF-MO 33

4.1.2 Adiabatic Potential Energy Surfaces 33

4.2 Excited State: $^1B_{2u}$ 35
4.2.1 Distincts of Different Point Groups 35
4.2.2 Dynamics of Symmetry Breaking 36
4.2.3 Electron Flux Associated with Symmetry Breaking 38
4.2.4 Radical Characters 40
4.2.5 Spectral Representation of the Electronic State Mixing 41
4.3 Excited State: $^1B_{1u}$ 44
4.4 Excited State: $^1B_{3u}$ 47
4.5 Conclusions 49

5 General Conclusions **52**

Appendix A **54**

Appendix B **56**

Acknownledgement **70**

Chapter 1

General Introduction

Woodward-Hoffmann Symmetry-forbidden Reaction and Nonadiabatic Effects

The molecular symmetry can be used to predict whether a reaction can occur or to elucidate the mechanism of one reaction. For example, according to the Woodward-Hoffmann rule (W-H rule) [1], by identifying the conservation of orbital symmetry with respect to a specified symmetry element, it is possible to predict whether or not the reaction along this direction can proceed. The W-H rule, with its universal and simple applicability, has become the basic law employed by the chemists.

At the same time, the originators of the rule also pointed out the limitation of its application. For example, before and after the reaction, the concerned symmetry element can not be destroied. Or that it would be rashly concluded that the reaction is symmetry-forbidden because that the orbital symmetry can not be conserved any more. However, the so-called symmetry-forbidden reactions may not necessarily be forbidden in the real world. Such a topic is of great significance for quantum mechanics and beyond the quantum chemistry which is built on the basis of the Born-Oppenheimer approximation (BO approximation) [2].

BO approximation was proposed by Born and Oppenheimer in 1927 when they applied quantum mechanics on the molecular system. In view of the fact that nuclei and electrons move in the different kinematic scales, the nuclei can be regarded as static when solve the electronic wavefunction. And then, under the fixed nuclear configuration, the corresponding eigenenergies and eigenfunctions of the electronic states can be solved to obtain the electronic potential energy surface, and accordingly the molecular properties as well as the chemical phenomena are discussed. So the quantum chemistry are also called "potential energy surface chemistry". Since the obtained PES is adiabatic or diabatic, if there is no external optical field, the electronic transition will not occur. As the modern computing technology has been developed, quantum chemistry has become an indispensable tool in the molecular science.

In fact, the original intention to propose BO approximation was due to the difficulty of calculating

the nuclei-electrons kinetic-coupling terms, e. g. $\langle \Phi_I | \partial_k \Phi_J \rangle$ which is also called nuclear derivative term and is reasonably ignored according to the physical reality. However, such a approximation is bound to fail sometimes. For example, when two or more PESs approach closely, the kinetic-coupling term becomes significant [3]. It likes the "friction" interaction among nuclei and electrons and via it the electrons gain the required energy from nuclear motion to carry out the nonadiabatic transition. To the present topic, given a symmetric molecular Hamiltonian, any symmetric operator belong to the point group should not break the molecular symmetry, which is the conservation of symmetry predicted by fundamental rules of quantum mechanics. However, reactants in fact often change their symmetries during a reaction, which is not strange to chemists. To deal with these phenomena, such nonadiabatic terms ignored by the BO approximation must be revived.

To understand the nuclei-electrons kinetic-coupling interactions, here is an example of classical mechanics employed to make an analogy. Concretely, compare the earth to the nuclei, and compare a satellite and the atmosphere to different electron states. As known, there are gravity and friction forces exist among the earth, the atmosphere, and the satellite. As the earth turns, if the satellite orbit is far from the atmosphere, friction between them is trivial and each object moves in its own orbit. But if the satellite and the atmosphere approach closely, the friction can be significant and finally affects the satellite orbit bit by bit till it falls. Apparently, if the earth is regarded as static or the friction is always ignored, these objects will move continually without alteration of their orbits. From this point of view, there are three factors causing satellite falling: the motion of the earth, the gravity and the friction forces.

If make an analogy in turn, it is easy to understand that there should be three factors to cause nonadiabatic transition in a molecular system: the nuclear motion, the Coulomb interaction, and the "friction" among nuclei and electrons. Wherein, the nuclear kinetic energy can be thought as the energy source and the Coulomb interaction especially the "friction" are necessary conditions. So the kinetic-coupling terms are crucial to the Woodward-Hoffmann symmetry-forbidden reaction. With the development of nonadiabatic dynamics theory, a further detailed analysis on the mechanism of these reactions has become possible and gave us motivation to do this work.

The History of Nonadiabatic Method

It may be better to make a brief introduction to the history of the nonadiabatic theory. The earliest theoretical study on nonadiabatic dynamics was by Landau [3], Zener [4] et al. when they studied the electron transfer process between two atoms in 1932. The Landau-Zener formula emulates the transition probability at the crossing point of two diabatic potential energy curves. As a development of it Zhu-Nakamura theory [5, 6] is able to deal with the avoided crossing area of the adiabatic potential curves. Yet they are one-dimensional. Semiclassical Ehrenfest theory (SET) [7,8] namely the mean-field theory is naturally multidimensional. However, it is not consistent with the

physical reality due to the artificial averaged nuclear path. The fewest switch surface hopping (FSSP) method [9] can avoid the difficulty faced by SET and thereby has become the most popular nonadiabatic method due to its easy-to-use. Yet it requires to distinguish individual potential energy surface in advance and that is difficult for the situation of densely degenerated electronic states.

As seen, the above mentioned nonadiabatic theories are still based on the PES information obtained by quantum chemistry methods and the time t is not yet explicitly included. Even the theoretical framework of time-dependent nonadiabatic dynamics had been established early in the 1930s, lots of kinds of approximations have to be assumed due to the difficulty of carrying out the "on-the-fly" scheme at the *ab initio* level.

What the "on-the-fly" means that the nuclear dynamics is driven by the electronic potential energy gradient. Considering the fact that the matter wave of nuclear is weak, it is reasonable to treat nuclei "classically". It is the so-called semiclassical theory which is as important as BO approximation to the molecular science. When the nonadiabatic effect is not obvious, such a scheme is well known as *ab initio* molecular dynamics (ABMD) which has been widely applied [10, 11].

So far, a brief summary can be made about the mentioned approximations. Firstly, without any approximation, the total molecular wave function can be expressed as

$$\Psi(\mathbf{r}, \mathbf{R}, t) = \sum_I \chi_I(\mathbf{R}, t)\Phi_I(\mathbf{r}; \mathbf{R}) \tag{1.1}$$

which called Born-Huang expansion [12]. Wherein χ and Φ are nuclear and electronic wavefunctions respectively. It is proposed according the fact that nuclei and electrons in a molecule are in the different kinematic scales. And it is mathematically complete. But due to the difficulty of solving the nuclei-electrons coupled terms, nuclei are regarded as static and then the electronic wave function can be obtained by solving the matrix equation

$$H^{\mathrm{el}}(\mathbf{r}; \mathbf{R})\Phi_I(\mathbf{r}; \mathbf{R}) = V_I(\mathbf{R})\Phi_I(\mathbf{r}; \mathbf{R}) \tag{1.2}$$

which is the so-called BO approximation. Wherein H^{el} is the electronic Hamiltonian. By virtue of BO approximation the adiabatic or diabatic potential energy surfaces can be obtained. And accordingly lots of nonadiabatic methods such as Landau-Zener formula, Zhu-Nakamura theory, and FSSP method etc. were proposed to deal with the crossing or avoided crossing areas where nonadiabatic effects are obvious. But the time t is not explicitly included so that these methods usually concentrate on estimating the nonadiabatic transition probability by virtue of the stationary potential energy surfaces. Considering that solving the time-dependent nuclear wavefunction is generally impossible except for the smallest molecular system, in order to describe the nuclear dynamics economically and consider the time t explicitly in the electronic wavepacket dynamics, the electronic state can be expressed as

$$\Psi(\mathbf{r}, t; \mathbf{R}(t)) = \sum_I C_I(t)\Phi_I(\mathbf{r}; \mathbf{R}(t)) \tag{1.3}$$

which is called semiclassical approximation because the collective nuclear positions are treated as "classical" parameters and the nuclear path is driven by the real-time electronic potential. However, the coupled terms are usually difficult to calculate.

When it comes to the present theme, what we need is not only a truly multidimensional on-the-fly method but also can deal with nuclei-electrons kinetic-coupling terms at the *ab initio* level. Such a work has been carried out over ten years in our group [13, 14]. At the early stage the nonadiabatic electronic wavepacket dynamics was carried by the mean field path and today the branching nuclear paths can also be tracked. These technologies have been applied to study the proton transfer dynamics [15], proton-electron transfer dynamics [16] and so on. In the present thesis, it is used to study the Woodward-Hoffmann symmetry-forbidden reaction, or say molecular spatial symmetry-breaking process.

The Present Work

As a case study the high symmetry molecule cyclic-B_4 was chosen. Along the directions of its six harmonic vibrational normal modes, there are various symmetry elements can be used. For example, during the ground state diamond-square-diamond (*dsd*) rearrangement process (see Chapter 2), all the symmetry elements of the D_{2h} point group (the stable geometry of this molecule is D_{2h}) can be maintained. However, the situation of excited states is complicated. The potential energy curves are densely degenerated that many crossing and avoided crossing points co-exist. In spite of tracking the same reaction coordinate, the molecular symmetry will be broken due to the passage of these areas. Such symmetry-breaking processes are usually accompanied by obvious nonadiabatic electronic transitions that have been known as Woodward-Hoffmann symmetry-forbidden reactions. However, how the transition occurs? What happened before the transition? It is the most important subject of this thesis that we want to emphasize.

To analyze the pre-transition process, a very useful quantum mechanics quantity of "electron flux" [17] is employed. It is a quantity that can be produced only by the complex wavefunctions which are used in the current electronic wavepacket dynamics. And it is an important feature that beyond quantum chemistry methods which use real wavefunctions.

Since we aim at clarifying the spatial symmetry-breaking mechanism by analyzing the nonadiabatic interactions, of necessity, the irreducible representations of molecule orbital bases should be idenified in advance. Instead of the self-consistent field (SCF) [18] procedures, the Hückel theory [19] is recalled to do such a work because the bond matrix in the Hückel method is thought to describe the bond nature of the molecule more concisely.

This thesis is organized as follows: as a preparation for dynamics study, analysis on the B_4 molecule by the quantum chemistry calculation including the Hückel theory is in chapter 2. Chapter 3 introduces the employed nonadiabatic theory and the way of implementation. In chapter 4 we

chose three excited states as initial states to carry out dynamics respectively. All of them are optical allowed transition from the ground state. Wherein the $^1B_{2u}$ excited state is particularly discussed in detail as an sample. A general conclusion is in chapter 5. Finally, as a reference, the Master's work [J. Phys. Chem. A 112 (2008) 9796, Bull. Korean Chem. Soc. 31 (2010) 895] is appended as Appendix B in which quantum chemistry methods are used to study the absorption and emission spectra of firefly oxyluciferin molecule in solvent in order to investigate the color-tuning mechanism in firefly luminescence, which is typical "potential energy surface chemistry".

Reference

[1] R. B. Woodward, and R. Hoffmann, J. Am. Chem. Soc. 87 (1965) 395.

[2] M. Born, and R. Oppenheimer, Ann. Phys. 84 (1927) 457.

[3] L. D. Landau, Phys. Z. Sowjetunion 2 (1932) 46.

[4] C. Zener, Proc. R. Soc. London. A 137 (1932) 696.

[5] C. Zhu, and H. Nakamura, J. Chem. Phys. 102 (1995) 7448.

[6] C. Zhu, and H. Nakamura, J. Chem. Phys. 106 (1997) 2599.

[7] M. V. Berry, and K. E. Mount, Rep. Prog. Phys. 35 (1972) 315.

[8] W. H. Miller, Adv. Chem. Phys. 25 (1974) 69.

[9] J. C. Tully, J. Chem. Phys. 93 (1990) 1061.

[10] H. Ushiyama, and K. Takatsuka, Angew. Chem. Int. Ed. 44 (2005) 1237.

[11] H. Ushiyama, and K. Takatsuka, Angew. Chem. Int. Ed. 46 (2007) 587.

[12] M. Born, and K. Huang, Dynamical Theory of Crystal Lattices (Oxford University Press: Oxford, 1954).

[13] T. Yonehara, K. Hanasaki, and K. Takatsuka, Chem. Rev. 112 (2012) 499.

[14] K. Takatsuka, T. Yonehara, K. Hanasaki, and Y. Arasaki, Chemical Theory beyond the Born-Oppenheimer Paradigm (World Scientific, Singpore, 2015).

[15] K. Nagashima, and K. Takatsuka, J. Phys. Chem. A 116 (2012) 11167.

[16] K. Yamamoto and K. Takatsuka, J. Chem. Phys. 140 (2014) 124111.

[17] L. I. Schiff, Quantum Mechanics (McGraw-Hill: New York 1968).

[18] A. Szabo, and N. S. Ostlund, Modern Quantum Chemistry (Dover Publishing, Mineola, New York, 1996).

[19] E. Hückel, Z. Phys. 70 (1931) 204.

Chapter 2

Choose B_4 as Case Study

2.1 Introduction

Boron atoms form various non-classical bonds to avoid empty $2p$ orbital left [1–3], which is important for chemists to develop valence structures theory. The concept of "3c-2e bond" proposed by Lipscomb and co-workers in 1954 [4] is a landmark work. It is very interesting to study not only the ground sate but also excited states of "electron-deficient" molecule, which owns more valence orbitals than electrons. Those irregular bonds lead to anomalous structures in ground state. The Lipscomb theory has successfully explained almost all the sorts of strange topological models of boranes [5], with the most famous example being diborane for the bridge hydrogen bond. The deltahedra structure has now been thought as the key unit for boron chemistry [6]. Among them, the compounds containing rhomboidal B_4 framework which was first noticed by Lipscomb in 1966 when he studied the fluxionality of boranes, is known as the so-called diamond-square-diamond (*dsd*) rearrangement (Fig. 2.1) [7]. It occurs by pseudo-rotation or pseudo-reflection process according to the detailed symmetry of individual polyhedra. In this conjunction several selection rules such as geometry-allowed (-forbidden) and orbital symmetry-allowed (-forbidden) have been reported in the frame of three-center theory [8–13].

Pure boron cluster B_4 as well as its ions are also studied both theoretically and experimentally [14–21]. Now it is widely recognized that the global minimum of neutral B_4 is singlet with D_{2h} geometry but not D_{4h} due to the pseudo-Jahn-Teller effect [14, 22]. We here simply call them cyclic-B_4 regardless of the global minimum. Its bonding characters, such as σ-π double aromaticity and *sp* hybridization have been discussed by high level *ab initio* calculations [17–19]. On the other hand, Reddy et al. simulated the photodetachment process of B_4^{-1} with considering nonadiabatic coupling between the ground and excited states [23, 24]. To the best of our knowledge, it is the only nonadiabatic electronic dynamics of B_4 reported so far. Besides, for their focus was vibrational cou-

pling, nuclear dynamics was limited within small displacements along normal modes. Considering the high symmetry of B_4, a real-time nonadiabatic excited state dynamics is anticipated. Take *dsd* process for example, and we readily observe a crossing of degenerate orbitals forming conical intersections and/or avoided crossings on the potential energy surfaces [2]. We here dynamically track those series of symmetry breaking with the method of nonadiabatic electron wavepacket dynamics. These dynamical processes constitute a theoretical foundation for chemical reaction theory for the class of the so-called symmetry forbidden reactions (in the terminology of Woodward-Hoffmann rule of conservation of orbital symmetry), in which symmetry-allowed conical intersections are usually involved. Therefore the present work serves also as a basic dynamical process of symmetry breaking (or mixing of electronic states belonging to different irreducible representations) caused by nonadiabatic interactions.

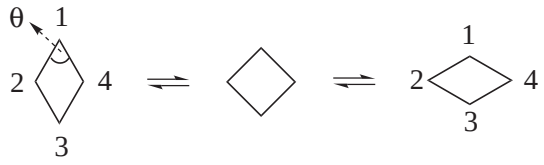

(a) Pseudo-rotation

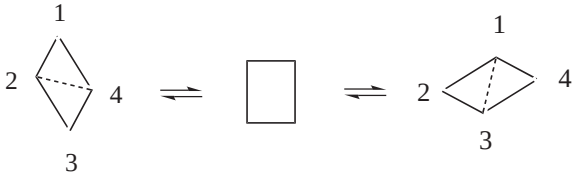

(b) Pseudo-reflection

FIG. 2.1: Diamond-square-diamond process. The angle B2-B1-B4 (θ) defines a reaction coordinate retaining D_{2h}.

Nonadiabatic electron wavepacket scheme is quite useful to track the electronic state dynamics [25]. In this theory, electron wavepackets are propagated and bifurcated along branching nuclear paths, which are in turn driven under the nonadiabatic couplings [26]. This general scheme is called the theory of phase space averaging and natural branching (PSANB) [27]. With the help of sophisticated ab initio quantum chemistry, tracking nonadiabatic electronic dynamics has now become feasible. However, it is quite often sufficient to track the electronic state mixing only along representative nuclear paths that are an average of those possible branching paths. This is the so-called semiclassical Ehrenfest theory, the theoretically correct form of which has been derived from the path-branching representation with correction terms that are missing from the intuitive way of

derivation [26]. These progresses have been employed to study several systems, such as bonding process of diborane [28], proton-electron transfer of Phenol-$(NH_3)_3$ and so on [29, 30]. (For more general scope and recent progress in the theory of nonadiabatic dynamics, see [27, 31–34].)

We begin the present studies with clarifying and visualizing orbital symmetry by applying the Hückel theory. Although nothing quantitatively accurate can be expected in this theory, it is still quite often useful for qualitative understanding of chemistry. Not only to see molecular orbital bases belonging to each irreducible representation, but also to locate a position of possible conical intersections we will see that the Hückel theory is still useful and instructive.

2.2 A Symmetry Consideration in Terms of the Hückel Theory

Since the study is on nonadiabatic electron wavepackets passing through the so-called symmetry-allowed conical intersections [35], it is needed beforehand to identify the irreducible representations of molecular symmetry and the spatial distribution of the bases of them.

2.2.1 Basic Bond Matrices

Writing a reasonable bond matrix is at the core of applying Hückel theory. The basis set chosen to carry out the Hückel calculations is as follows. According to the previous studies, it is convenient to reorient three $2p$ orbitals of boron into radial (p_r), tangential (p_t) and perpendicular (p_π) sets [18,36]. With $2s$, we have four trial models primarily to be considered (Fig. 2.2).

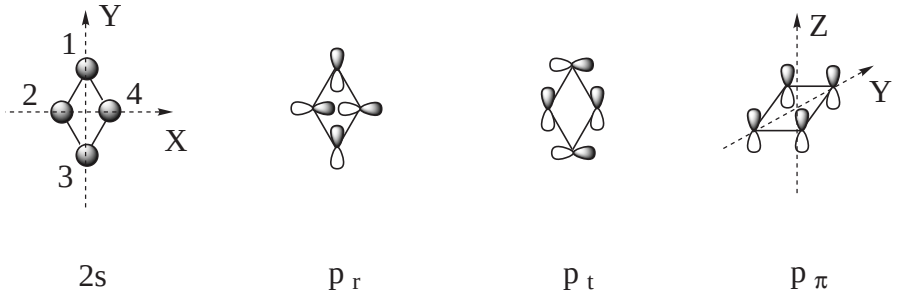

FIG. 2.2: Trial basis sets for Hückel method

One may doubt that whether or not such a grouping is reasonable since it disregards mixing among different models. It is just the thing to be answered after relative discussions later. So, by setting the Coulomb integrals of each set of bases to α and resonance integrals of edges are to β

(positive overlap) or $-\beta$ (negative overlap), corresponding bond matrices are

$$2s,\ p_\pi = \begin{bmatrix} -\lambda & 1 & a & 1 \\ 1 & -\lambda & 1 & b \\ a & 1 & -\lambda & 1 \\ 1 & b & 1 & -\lambda \end{bmatrix},\ p_t = \begin{bmatrix} -\lambda & -1 & a & 1 \\ -1 & -\lambda & 1 & b \\ a & 1 & -\lambda & -1 \\ 1 & b & -1 & -\lambda \end{bmatrix},\ p_r = \begin{bmatrix} -\lambda & -1 & -a & 1 \\ -1 & -\lambda & 1 & -b \\ -a & 1 & -\lambda & -1 \\ 1 & -b & -1 & -\lambda \end{bmatrix}, \tag{2.1}$$

where

$$-\lambda = \frac{\alpha - \varepsilon}{\beta} \tag{2.2}$$

while ε is energy eigenvalue, and relative definitions are

$$\alpha_r = \int \chi_r \hat{h} \chi_r d\tau, \tag{2.3}$$

$$\beta_{rs} = \int \chi_r \hat{h} \chi_s d\tau, \tag{2.4}$$

and

$$\varepsilon = \frac{\int \varphi \hat{h} \varphi d\tau}{\int \varphi \varphi d\tau}, \tag{2.5}$$

wherein $\hat{h}$ is 1-e effective Hamiltonian

$$\hat{h} = -\frac{\hbar^2}{2m_e}\nabla^2 + V(\vec{r}). \tag{2.6}$$

and φ is just the eigenfunction need to be solved; χ_r is AO basis.

Unusual parameters $a\beta$ and $b\beta$ are introduced to describe the bondings B1-B3 and B2-B4. Generally, they are ignored when apply Hückel method to cyclic-compounds, such as for benzene and cyclicbutane but be considered here in advance. In addition, the minus sign before resonance integral usually does not appear in bond matrix. Writing them outside is to emphasize the anti-bonding character between two bases. Note that $2s$, p_π and p_r have the same determinant as

$$\mathbf{det}(2s,\ \mathrm{p}_\pi,\ \mathrm{p}_r) = \lambda^4 - (a^2 + b^2 + 4)\lambda^2 - (4a + 4b)\lambda + a^2b^2 - 4ab, \tag{2.7}$$

while for p_t it is

$$\mathbf{det}(\mathrm{p}_t) = \lambda^4 - (a^2 + b^2 + 4)\lambda^2 + (4a + 4b)\lambda + a^2b^2 - 4ab \tag{2.8}$$

which implies the special role of p_t model.

Suppose β varies in 4-order inverse proportion to nuclear distance [37] during *dsd* and bond lengths of edges are set equal to constant 1, a and b are given as $(2\cos\theta/2)^{-4}$ and $(2\sin\theta/2)^{-4}$ with use of the angle defined in Fig. 2.1. Vary θ, the geometric variation on bond combination during *dsd* process can be investigated (Fig. 2.3). Since β is negative so the value of $-\lambda$ in fact indicates orbital energy. It can be seen that only p_t gives three bonding orbitals, while each of the rest sets of $2s$, p_r and p_π, has merely one bonding orbital to be available

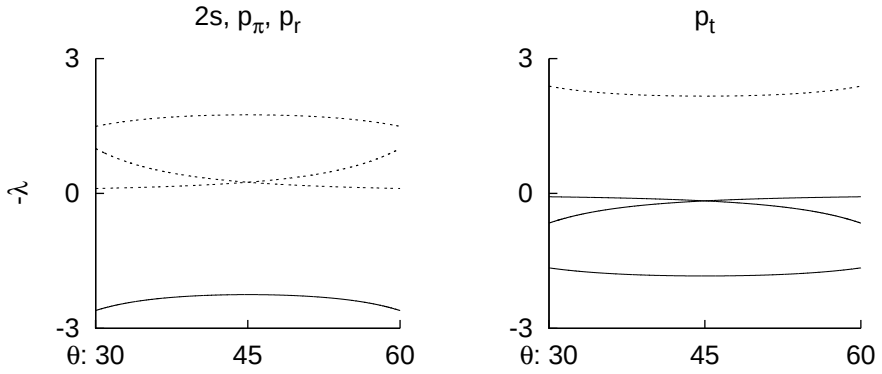

FIG. 2.3: Geometric variation on $-\lambda$ of $2s$, p_r, p_π and p_t sets along $\omega_1(A_g)$ mode predicted by Hückel theory.

2.2.2 Description of *sp* Hybridization in the Hückel framework

Since there are 12 valence electrons involved in $2s$ and $2p$ atomic orbitals, *sp* hybridization is a key to perform good calculation in the Hückel framework. *sp* hybridization of the cyclic-B_4 has been studied with the extended Hückel method as well as *ab initio* calculations with large basis sets [18, 36]. By the extended Hückel method [38], Hoffman et al. have shown that the degenerate orbitals at square are mixing of s, p_t and p_r. Wang et al. found that among six occupied valence orbitals, the highest three ones are typical p_r, p_π and p_t, while the lowest three ones are mainly $2s$ with hybridization of p_r or p_t, respectively (6-311+g(2df) basis set). But the other $2s$-based orbital becomes anti-bonding and hence unoccupied [19].

Further, $2s$-p_t hybridization is given as

$$\begin{aligned} \varphi_1 &= \tfrac{\sqrt{2}}{2}2s + \tfrac{\sqrt{2}}{2}2p_{x(y)} \\ \varphi_2 &= \tfrac{\sqrt{2}}{2}2s - \tfrac{\sqrt{2}}{2}2p_{x(y)}, \end{aligned} \tag{2.9}$$

which are depicted in Fig. 2.4,

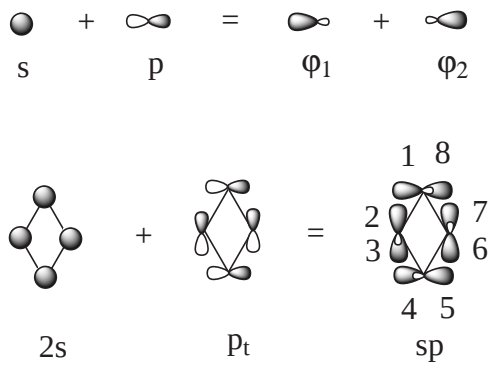

FIG. 2.4: $2s$-p_t hybridization for Hückel method

with corresponding bond matrix is

$$sp = \begin{bmatrix} -\lambda & 1 & 0 & a & 0 & 0 & 0 & 0 \\ 1 & -\lambda & 0 & 0 & 0 & 0 & b & 0 \\ 0 & 0 & -\lambda & 1 & 0 & b & 0 & 0 \\ a & 0 & 1 & -\lambda & 0 & 0 & 0 & 0 \\ 0 & 0 & 0 & 0 & -\lambda & 1 & 0 & a \\ 0 & 0 & b & 0 & 1 & -\lambda & 0 & 0 \\ 0 & b & 0 & 0 & 0 & 0 & -\lambda & 1 \\ 0 & 0 & 0 & 0 & a & 0 & 1 & -\lambda \end{bmatrix}. \tag{2.10}$$

Together with original p_r and p_π sets, in D_{2h} point group of B_4 they are decomposed into

$$\begin{aligned} \Gamma_{p_\pi} &= b_{2g} \oplus b_{3g} \oplus 2b_{1u} \\ \Gamma_{p_r} &= 2a_g \oplus b_{2u} \oplus b_{3u} \\ \Gamma_{sp} &= 2a_g \oplus 2b_{1g} \oplus 2b_{2u} \oplus 2b_{3u} \end{aligned} \tag{2.11}$$

In this way, twelve valence electrons fill into six bonding orbitals comfortably, while p_r and p_π are typical 4c-2e bonds (see Fig. 2.5). Besides, four degenerated pairs at the square are well reproduced. If parameters a and b are set to zero, the degenerated orbitals of p_r and p_π would become non-bonding at all and even distortion could not separate them, which obviously destructs all the results reported. So the interaction between para-atoms is important for cyclic-B_4, even though they may be weak. Finally, after summing up occupied orbital energies of sp, as well as p_r and p_π, D_{4h} is still at the maximum, and the electronic potential favors to distort this molecule.

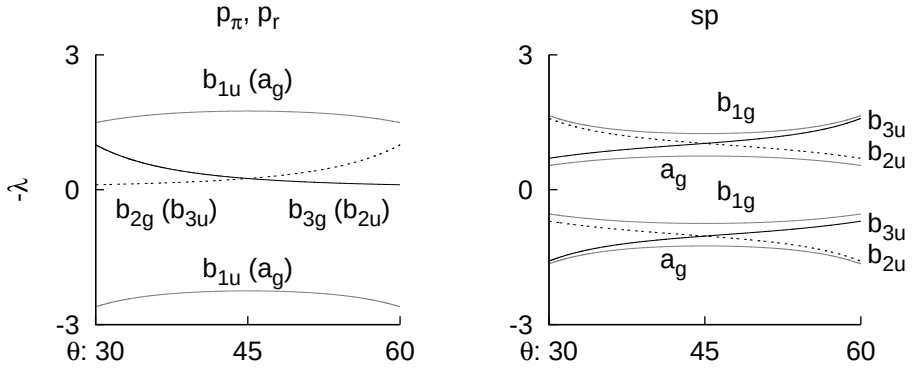

FIG. 2.5: Geometric variation on $-\lambda$ of p_r, p_π and sp sets along $\omega_1(A_g)$ mode predicted by Hückel theory.

As seen, pesudo-rotation path relates to $\omega_1(A_g)$ mode. For excited study later, pesudo-reflection path which relates to $\omega_6(B_{1g})$ is also simulated in the similar way. The character table is then

changed into C_{2h} and the irreducible representations are decomposed into

$$\begin{aligned} \Gamma_{\mathrm{p}_\pi} &= 2b_g \oplus 2a_u \\ \Gamma_{\mathrm{p}_r} &= 2a_g \oplus 2b_u \\ \Gamma_{sp} &= 4a_g \oplus 4b_u \end{aligned} \tag{2.12}$$

Assumptions are also changed (see Fig. 2.6):

1. The variable is the bond length of B1-B2 with initial value of 1.
2. θ is invariable.
3. Initial $\delta = 50°$.

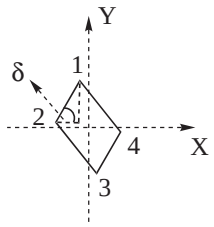

FIG. 2.6: Diagram of $\omega_6(B_{1g})$ vibration used for Hückel treatment.

As a result, solutions of $-\lambda$ are exhibited in Fig. 2.7. Crossed orbitals in $\omega_1(A_g)$ direction become to avoided crossing along this path.

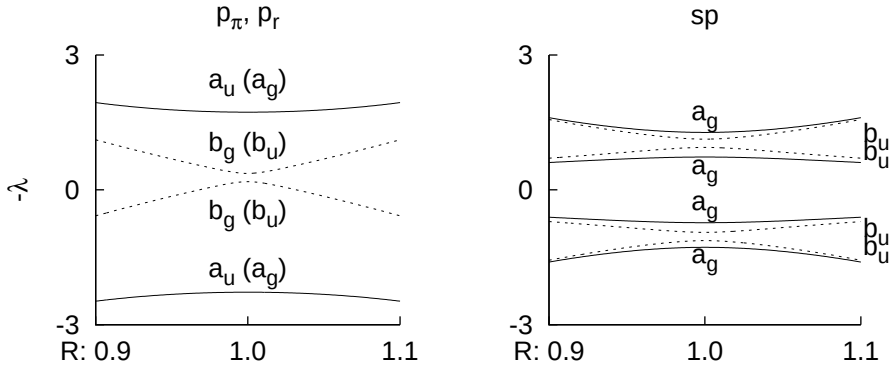

FIG. 2.7: Geometric variation on $-\lambda$ of p_π, p_r and sp sets along $\omega_6(B_{1g})$ mode predicted by Hückel theory.

2.2.3 Hückel Molecular Orbitals As the Bases of Irreducible Representations

As λ is known, molecular orbital can be solved simultaneously. Firstly, symmetric functions of each irreducible representation are listed as below:

p_π

$$\begin{aligned}
\psi(b_{2g}) &= \tfrac{\sqrt{2}}{2}(\chi_2 - \chi_4) \\
\psi(b_{3g}) &= \tfrac{\sqrt{2}}{2}(\chi_1 - \chi_3) \\
\psi_1(b_{1u}) &= \tfrac{\sqrt{2}}{2}(\chi_1 + \chi_3) \\
\psi_2(b_{1u}) &= \tfrac{\sqrt{2}}{2}(\chi_2 + \chi_4),
\end{aligned} \tag{2.13}$$

p_r

$$\begin{aligned}
\psi_1(a_g) &= \tfrac{\sqrt{2}}{2}(\chi_1 - \chi_3) \\
\psi_2(a_g) &= \tfrac{\sqrt{2}}{2}(\chi_2 - \chi_4) \\
\psi(b_{2u}) &= \tfrac{\sqrt{2}}{2}(\chi_1 + \chi_3) \\
\psi(b_{3u}) &= \tfrac{\sqrt{2}}{2}(\chi_2 + \chi_4),
\end{aligned} \tag{2.14}$$

sp

$$\begin{aligned}
\psi_1(a_g) &= \tfrac{1}{2}(\varphi_1 + \varphi_4 + \varphi_5 + \varphi_8) \\
\psi_2(a_g) &= \tfrac{1}{2}(\varphi_2 + \varphi_3 + \varphi_6 + \varphi_7) \\
\psi_1(b_{1g}) &= \tfrac{1}{2}(\varphi_1 - \varphi_4 + \varphi_5 - \varphi_8) \\
\psi_2(b_{1g}) &= \tfrac{1}{2}(\varphi_2 - \varphi_3 + \varphi_6 - \varphi_7) \\
\psi_1(b_{2u}) &= \tfrac{1}{2}(\varphi_1 - \varphi_4 - \varphi_5 + \varphi_8) \\
\psi_2(b_{2u}) &= \tfrac{1}{2}(\varphi_2 - \varphi_3 - \varphi_6 + \varphi_7) \\
\psi_1(b_{3u}) &= \tfrac{1}{2}(\varphi_1 + \varphi_4 - \varphi_5 - \varphi_8) \\
\psi_2(b_{3u}) &= \tfrac{1}{2}(\varphi_2 + \varphi_3 - \varphi_6 - \varphi_7).
\end{aligned} \tag{2.15}$$

Notice the atomic orbital bases are χ for p_π and p_r while φ for *sp* (refer to Fig. 2.2 and Fig. 2.4). Then, substitute them into secular equation **HC=CE**, and the following equations are obtained:

p_π

$$\begin{bmatrix} -\lambda - b & 0 \\ 0 & -\lambda - a \end{bmatrix} \begin{bmatrix} c(b_{2g}) \\ c(b_{3g}) \end{bmatrix} = 0 \tag{2.16}$$

$$\begin{bmatrix} -\lambda + a & 2 \\ 2 & -\lambda + b \end{bmatrix} \begin{bmatrix} c_1(b_{1u}) \\ c_2(b_{1u}) \end{bmatrix} = 0, \tag{2.17}$$

p_r

$$\begin{bmatrix} -\lambda + a & -2 \\ -2 & -\lambda + b \end{bmatrix} \begin{bmatrix} c_1(a_g) \\ c_2(a_g) \end{bmatrix} = 0 \tag{2.18}$$

$$\begin{bmatrix} -\lambda - a & 0 \\ 0 & -\lambda - b \end{bmatrix} \begin{bmatrix} c(b_{2u}) \\ c(b_{3u}) \end{bmatrix} = 0, \tag{2.19}$$

sp

$$\begin{bmatrix} -\lambda + a & 1 \\ 1 & -\lambda + b \end{bmatrix} \begin{bmatrix} c_1(a_g) \\ c_2(a_g) \end{bmatrix} = 0 \tag{2.20}$$

$$\begin{bmatrix} -\lambda - a & 1 \\ 1 & -\lambda - b \end{bmatrix} \begin{bmatrix} c_1(b_{1g}) \\ c_2(b_{1g}) \end{bmatrix} = 0 \tag{2.21}$$

$$\begin{bmatrix} -\lambda - a & 1 \\ 1 & -\lambda + b \end{bmatrix} \begin{bmatrix} c_1(b_{2u}) \\ c_2(b_{2u}) \end{bmatrix} = 0 \tag{2.22}$$

$$\begin{bmatrix} -\lambda + a & 1 \\ 1 & -\lambda - b \end{bmatrix} \begin{bmatrix} c_1(b_{3u}) \\ c_2(b_{3u}) \end{bmatrix} = 0. \tag{2.23}$$

To get non-zero $\mathbf{C}$, determinant of $\mathbf{H}$ need to be zero and thus λ are determined. With normality conditions, $\mathbf{C}$ are solved easily. Finally, combine $\mathbf{C}$ with corresponding symmetric bases from Eq. (2.13) to Eq. (2.15), Hückel molecular orbitals are determined.

Take $\theta = 80°$ for example, molecular orbital coefficients and diagrams are shown in Table 2.1 and Fig. 2.8.

Table 2.1: Hückel-MO coefficients ζ, as well as $-\lambda$, at geometry of $\theta = 80°$.

	p_π				p_r			
	b_{1u}	b_{3g}	b_{2g}	b_{1u}	a_g	b_{2u}	b_{3u}	a_g
$-\lambda$	-2.276	0.181	0.366	1.728	-2.276	0.181	0.366	1.728
ζ_1	0.488	0.707	0.000	0.511	0.488	0.707	0.000	0.511
ζ_2	0.511	0.000	0.707	-0.488	-0.511	0.000	0.707	0.488
ζ_3	0.488	-0.707	0.000	0.511	-0.488	0.707	0.000	-0.511
ζ_4	0.511	0.000	-0.707	-0.488	0.511	0.000	0.707	-0.488

	sp							
	a_g	b_{2u}	b_{3u}	b_{1g}	a_g	b_{2u}	b_{3u}	b_{1g}
$-\lambda$	-1.278	-1.129	-0.944	-0.730	0.730	0.944	1.129	1.278
ζ_1	0.337	0.303	0.398	0.369	0.369	0.398	0.303	0.337
ζ_2	0.369	0.398	0.303	0.337	-0.337	-0.303	-0.398	-0.369
ζ_3	0.369	-0.398	0.303	-0.337	-0.337	0.303	-0.398	0.369
ζ_4	0.337	-0.303	0.398	-0.369	0.369	-0.398	0.303	-0.337
ζ_5	0.337	-0.303	-0.398	0.369	0.369	-0.398	-0.303	0.337
ζ_6	0.369	-0.398	-0.303	0.337	-0.337	0.303	0.398	-0.369
ζ_7	0.369	0.398	-0.303	-0.337	-0.337	-0.303	0.398	0.369
ζ_8	0.337	0.303	-0.398	-0.369	0.369	0.398	-0.303	-0.337

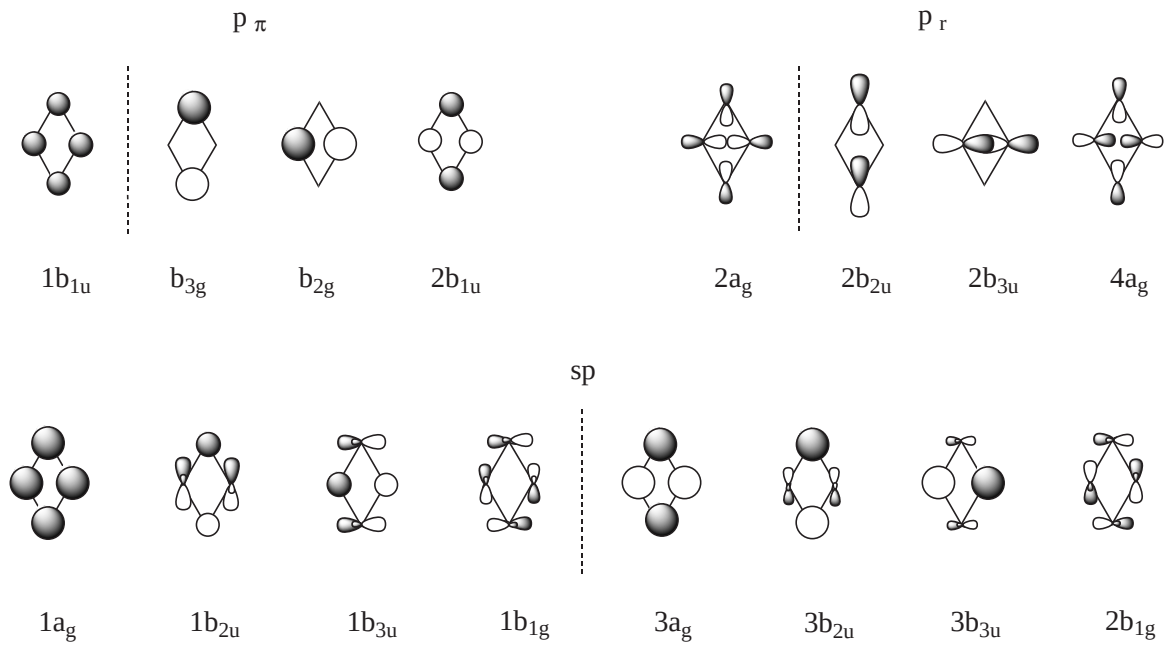

FIG. 2.8: The Hückel MOs arising from the independent basis sets. Bonding and anti-bonding orbitals are separated by dotted lines.

2.2.4 Symmetry-allowed Conical Intersections Foreseen with the Hückel Theory

We henceforth concentrate on the dynamics starting from D_{2h} (diamond shape) with the initial reaction coordinate θ as in Fig. 2.1. Figure 2.9(a) displays the θ-dependence of the orbital energies of the selected Hückel MO's, which are relevant to the low-lying excited states. The orbital energies have been calculated with the following parameters: $H_{rr}(2s) = -15.2$ eV, $H_{rr}(2p) = -8.5$ eV, $H_{rs} = (K/2)S_{rs}(H_{rr} + H_{ss})$, $K = 1.75$ [38]. The overlap integrals S_{rs} are borrowed from those of STO-3G basis sets with bond length of edges fixed at 1.5 Å. The irreducible representations denoted there should be referred to as in Fig. 2.8.

In terms of these MOs, we next attempt to draw the θ-dependent curve of the relevant excitation energies of single excitation. As known well, the excitation energy $\Delta E_{i\to a}$ from an occupied MO i to an unoccupied one a is estimated with a simple formula

$$\Delta E_{i\to a} = (E_0 - \epsilon_i + \epsilon_a) - E_0 = \epsilon_a - \epsilon_i, \tag{2.24}$$

where E_0 is the Hückel ground state energy. The orbital energies can be seen as above in Fig. 2.9(a). The spin multiplicity is out of the scope of the Hückel framework. Figure 2.9(b) shows the resultant potential energy curve along θ. Since the configurations of excitation to $2b_{3u}$ and b_{2g} are not included, only curves are displayed there that basically increase as θ.

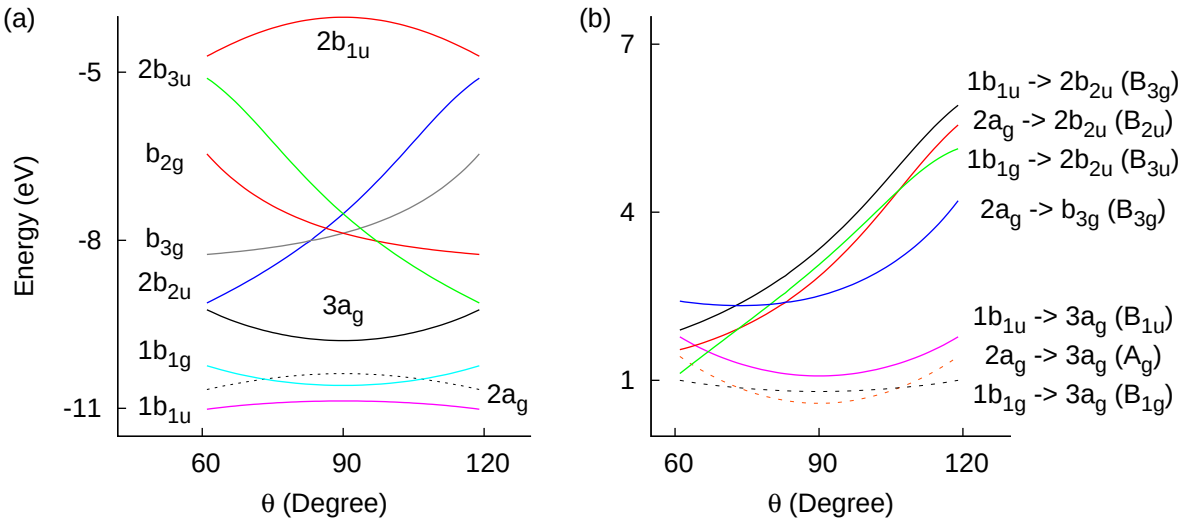

FIG. 2.9: (a) Hückel MO energy in the mode of $\omega_1(A_g)$ along the reaction coordinate θ. Those below $1b_{1u}$ and high-lying than $2b_{1u}$ are omitted in this panel. (b) Excitation energies for the selected excited states estimated with the Hückel MO energies as presented in panel (a). The configurations of excitation to $2b_{3u}$ and b_{2g} are not included, which are responsible for the reflection symmetry with respect to $\theta = 90°$. These features are to be compared with the *ab initio* adiabatic potential curves of Fig. 4.2.

Each of the curves in this panel is labeled in terms of the excitation configuration $i \rightarrow a$ along with the resultant symmetry of the total wavefunction. We observe many crossings between the curves. Except for that between the states of $2a_g \rightarrow b_{3g}$ (B_{3g}) and $1b_{1u} \rightarrow 2b_{2u}$ (B_{3g}), every crossing represents a symmetry-allowed conical intersection. The crossing between these two B_{3g} states should be avoided along this one-dimensional coordinate (ω_1 mode), but the Hückel theory assigns it to be a direct crossing (due to an exact degeneracy), since these are treated as pseudo-diabatic wavefunctions.

This diagram of the excitation energy should be compared with Fig. 4.2, in which the similar potential curves are reproduced with the *ab initio* Configuration Interaction calculations. The comparison should be made in the range of the angle θ smaller than 90°. Reasonable but only qualitative agreement is seen with respect to the presence of the conical intersections. Although it is too much to demand the Hückel theory to provide accurate information regarding the location (angle here) and energy of the crossing points, it is yet instructive to use the Hückel theory for understanding the mechanism and guessing the positions of conical intersections. Indeed we will refer to the conical intersections found here in the later study to characterize the nonadiabatic dynamics of symmetry breaking. This situation reminds of the Walsh rule based on the Hückel theory to predict whether the molecular shape of AB_2 type is linear or bent.

Reference

[1] W. N. Lipscomb, Science 196 (1977) 1047.

[2] R. B. King, Chem. Rev. 101 (2001) 1119.

[3] E. Osorio, J. K. Olson, W. Tiznado, and A. I. Boldyrev, Chem.-A Eur. J. 18 (2012) 9677.

[4] W. H. Eberhardt, B. Crawford, and W. N. Lipscomb, J. Chem. Phys. 22 (1954) 989.

[5] W. N. Lipscomb, Boron Hydrides (W. A. Benjamin. Inc, New York, 1963).

[6] R. E. Williams, Inorg. Chem. 10 (1971) 210.

[7] W. N. Lipscomb, Science 153 (1966) 373.

[8] D. A. Kleier, and W. N. Lipscomb, Inorg. Chem. 18 (1979) 1312.

[9] B. M. Gimarc, and J. J. Ott, Inorg. Chem. 25 (1986) 2708.

[10] B. M. Gimarc, and J. J. Ott, Inorg. Chem. 25 (1986) 83.

[11] R. B. King, Inorg. Chim. Acta. 49 (1981) 237.

[12] D. Michael, P. Mingos, and R. L. Johnston, Polyhedron 7 (1988) 2437.

[13] D. J. Wales, and A. J. Stone, Inorg. Chem. 26 (1987) 3845.

[14] J. M. L. Martin, J. P. Franois, and R. Gijbels, Chem. Phys. Lett. 189 (1992) 529.

[15] H. Kato, and E. Tanaka, J. Comput. Chem. 12 (1991) 1097.

[16] H. Reis, and M. G. Papadopoulos, J. Comput. Chem. 20 (1999) 679.

[17] H. Jin, and Q. Li, Phys. Chem. Chem. Phys. 5 (2003) 1110.

[18] H. Zhai, L. Wang, A. N. Alexandrova, A. I. Boldyrev, and V. G. Zakrzewski, J. Phys. Chem. A 107 (2003) 9319.

[19] A. N. Alexandrova, A. I. Boldyrev, H. Zhai and L. Wang, Coord. Chem. Rev. 250 (2006) 2811.

[20] R. Linguerri, I. Navizet, P. Rosmus, S. Carter, and J. P. Maier, J. Chem. Phys. 122 (2005) 034301.

[21] M. Hatanaka, J. Mol. Struct.: {THEO} 942 (2010) 55.

[22] R. G. Pearson, J. Am. Chem. Soc. 91 (1969) 4947.

[23] S. R. Reddy, and S. Mahapatra, J. Chem. Phys. 136 (2012) 024322.

[24] S. R. Reddy, and S. Mahapatra, J. Chem. Phys. 136 (2012) 024323.

[25] T. Yonehara, K. Hanasaki, and K. Takatsuka, Chem. Rev. 112 (2012) 499.

[26] T. Yonehara, and K. Takatsuka, J. Chem. Phys. 128 (2008) 154104.

[27] K. Takatsuka, T. Yonehara, K. Hanasaki, and Y. Arasaki, Chemical Theory beyond the Born-Oppenheimer Paradigm (World Scientific, Singpore, 2015).

[28] T. Yonehara, and K. Takatsuka, Chem. Phys. 366 (2009) 115.

[29] K. Nagashima, and K. Takatsuka, J. Phys. Chem. A 113 (2009) 15240.

[30] K. Nagashima, and K. Takatsuka, J. Phys. Chem. A 116 (2012) 11167.

[31] A. Jasper, B. K. Kendrick, C. A. Mead, and D. G. Truhlar, in Modern Trends in Chemical Reaction Dynamics (X. Yang and K. Liu Ed., World Scientific, Singapore, 2004).

[32] W. Domcke, D. R. Yarkony, and H. Köppel, Conical Intersections (World Scientific, Singapore, 2004).

[33] T-S. Chu, Y. Zhang, and K-L. Han, Int. Rev. Phys. Chem. 25 (2006) 201.

[34] H. Nakamura, Nonadiabatic Transition: Concepts, Basic Theories and Applications, 2nd Ed. (World Scientific, Singapore, 2012).

[35] Conical Intersections (Ed. W. Domcke, D. R. Yarkony, H. Köppel, World Scientific, 2004).

[36] M. M. Balakrishnarajan, and R. Hoffmann, J. Am. Chem. Soc. 126 (2004) 13119.

[37] C. Sandorfy, Bull. Soc. Chim.France 615 (1949).

[38] R. Hoffmann, J. Chem. Phys. 39 (1963) 1397.

Chapter 3

Theoretical Methods and Implementation

3.1 Theoretical Background

The theoretical frame we work with to propagate nonadiabatic electron dynamics is outlined first along with illustrative quantities to highlight the resultant dynamics. The mass-weighted coordinates are used throughout.

3.1.1 Nonadiabatic Electronic Dynamics

The electronic state is expressed by

$$\Psi(\mathbf{r},t;\mathbf{R}(t)) = \sum_{I}^{\mathrm{CSF}} C_I(t)\Phi_I(\mathbf{r};\mathbf{R}(t)) \tag{3.1}$$

which means that the electronic wavepackets are propagated along a nuclear path $\mathbf{R}(t)$. Basis functions $\Phi_I(\mathbf{r};\mathbf{R}(t))$ can be rather arbitrary but here we adopt configuration state functions (CSF), which are assumed to be orthonormal at each nuclear configuration. The time-dependent variational principle for the Schrödinger equation gives coupled equations of motion for the coefficients $\{C_I(t)\}$ are [1]

$$i\hbar\frac{\partial}{\partial t}C_I = \sum_{J}^{\mathrm{CSF}}\left(H_{IJ}^{(el)} - i\hbar\sum_{k}^{\mathrm{nuc}}\dot{R}_k X_{IJ}^k - \frac{\hbar^2}{4}\sum_{k}^{\mathrm{nuc}}(Y_{IJ}^k + Y_{JI}^{k^*})\right)C_J \tag{3.2}$$

wherein

$$H_{IJ}^{(el)} = \left\langle \Phi_I \left| \hat{H}^{(el)} \right| \Phi_J \right\rangle, \quad X_{IJ}^k = \left\langle \Phi_I \left| \frac{\partial}{\partial R_k} \right| \Phi_J \right\rangle \quad \text{and} \quad Y_{IJ}^k = \left\langle \Phi_I \left| \frac{\partial^2}{\partial R_k^2} \right| \Phi_J \right\rangle. \tag{3.3}$$

Note that the second-order terms Y_{IJ}^k are missing in the conventional form of the SET. We here neglect these terms throughout this work anyway, which is justified by the presence of $\hbar^2$. In what

follows, the expectation values represented in terms of the ket and bra vectors indicate integration over only the electronic coordinates.

Obviously, the first term in the right-hand side of Eq. (3.2) comes from interactions among electronic states, while the second and third terms represent the kinematic couplings with the motion of nuclei. Since CSFs form a quasi-diabatic basis set, most of nonadiabatic effects are actually contributed from the first term. In case where $\hat{H}^{(el)}$ happens to have a symmetry at a given molecular geometry, the adiabatic electronic states (in the Born-Oppenheimer approximation) belonging to different irreducible representations are not mixed together by $H_{IJ}^{(el)}$, and spatial-symmetry breaking is realized only through X_{IJ}^{k}. Therefore nuclear motions as those in the vibrational modes can cause the electronic state mixing of different symmetries, and the initial electronic wavefunction of an irreducible representation can be contaminated by other electronic states of different irreducible representation, which we refer to as symmetry-breaking. Thus the nuclear kinematic coupling terms are critically important in this work.

3.1.2 Nonadiabatic Nuclear Dynamics

The nuclear path solutions $\mathbf{R}(t)$ are obtained with the Euler-Lagrange variational principle, which bring about the force matrix $\mathbf{F}(\mathbf{R})$ [2], a matrix representation of the force operator $\hat{\mathcal{F}}^{k}$ to drive the nuclear motion in the kth direction, which is defined as

$$\begin{aligned}\mathbf{F}_{IJ}^{k} &= \langle\Phi_I|\hat{\mathcal{F}}^{k}|\Phi_J\rangle \\ &= -\left[\frac{\partial H_{IJ}^{(el)}}{\partial R_k} + \sum_K \left(X_{IK}^{k} H_{KJ}^{(el)} - H_{IK}^{(el)} X_{KJ}^{k}\right)\right] \\ &\quad + i\hbar \sum_l \dot{R}_l \left[\frac{\partial X_{IJ}^{l}}{\partial R_k} - \frac{\partial X_{IJ}^{k}}{\partial R_l}\right]. \end{aligned} \tag{3.4}$$

If the basis functions were complete, this matrix element becomes dramatically simpler as

$$\mathbf{F}_{IJ}^{k} = \langle\Phi_I|\frac{\partial H^{(el)}}{\partial R_k}|\Phi_J\rangle. \tag{3.5}$$

Note that if the off-diagonal matrix elements X_{IJ}^{k} are negligibly small in the adiabatic representation, the force matrix has only the diagonal elements, which are equivalent to the ordinary forces given by the energy gradients of the individual potential energy surfaces (or the Hellmann-Feynman forces). If X_{IJ}^{k} is not small, on the other hand, the nuclear motion coupled with the dynamics of electronic-state mixing can branch into many pieces in a cascade manner, mimicking the nuclear wavepacket bifurcation and deformation. The paths thus branching eventually proceed to their individual adiabatic potential surfaces, which are usually specified in terms of the electronic state symmetry in spectroscopic notations. After all, the total wavefunction is represented by coherent superposition of those branching pieces of electronic and nuclear wavefunctions. (See the examples of full quantum electronic and nuclear quantum calculations of wavepacket bifurcation through avoided crossing in

refs. [3, 4] and conical intersections in [5, 6], and the relevant experimental observation in [7].) Such a wavepacket bifurcation can be well described in mixed quantum and classical representation, the algorithms of which are provided in refs. [8–11].

The mean-field paths in the SET [12–17] appear to be as a special case of the present theory if we take a force average in the kth direction over the electron wavepacket such that

$$\begin{aligned}\ddot{\mathbf{R}}^k &= \langle\Psi(\mathbf{r},\mathbf{R},t)|\hat{\mathcal{F}}^k|\Psi(\mathbf{r},\mathbf{R},t)\rangle = \sum_{I,J} C_I^* \mathbf{F}_{IJ}^k C_J \\ &= -\sum_{I,J,K} C_I^* \left(X_{IK}^k H_{KJ}^{(el)} - H_{IK}^{(el)} X_{KJ}^k \right) C_J - \sum_{IJ} C_I^* \frac{\partial H_{IJ}^{(el)}}{\partial R_k} C_J, \end{aligned} \tag{3.6}$$

which is equivalent to the Hellmann-Feynman force

$$\ddot{\mathbf{R}}^k = -\left\langle \Psi(\mathbf{R}(t)) \left| \frac{\partial H^{(el)}}{\partial R_k} \right| \Psi(\mathbf{R}(t)) \right\rangle, \tag{3.7}$$

only if the electronic basis set happens to be complete.

To reproduce branching nuclear paths, more faithful treatment of the force matrix is needed. In fact, developed progresses have been reported both in theoretical and experimental aspects [3, 4, 9, 18, 19]. But for the present work, tracking the branching paths is not our focus in this particular study. B_4 has six vibrational normal modes (Fig. 3.1) and each relates to its own irreducible representation orbitals. Therefore this paper is devoted to observation of the way how these normal modes can be mixed up together as the total electron wavepackets develop through the nuclear kinematic couplings.

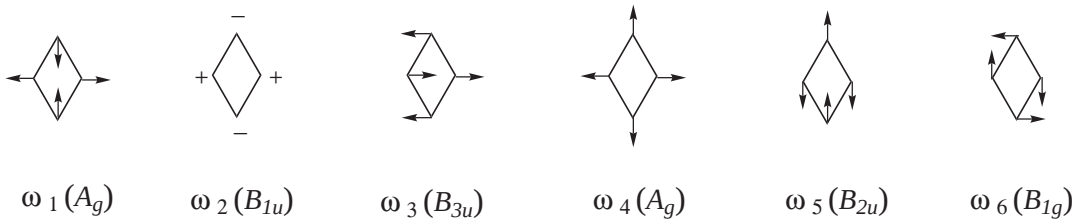

FIG. 3.1: Normal modes of vibration of *rhombo*-B_4.

3.1.3 Electron Flux Analysis

The dynamical flow of electrons within a molecule can be directly monitored in terms of the probability current density $\vec{j}(\mathbf{r},t)$ that satisfies the continuity equation

$$\frac{\partial \rho(\mathbf{r},t)}{\partial t} + \nabla \vec{j}(\mathbf{r},t) = 0. \tag{3.8}$$

In quantum mechanics $\vec{j}(\mathbf{r},t)$ is defined as

$$\vec{j}(\mathbf{r},t) = \frac{\hbar}{2im_e}[\psi^* \nabla\psi - \psi \nabla\psi^*] \tag{3.9}$$

which we simply call Schiff flux [20], where m_e and ψ are the mass and wave function of the involved particles. For many-electron systems it is redefined as

$$\begin{aligned}\vec{j}(\mathbf{r},t) &= \frac{\hbar}{2im_e}[\nabla_{\mathbf{r}}\gamma(\mathbf{r}',\mathbf{r}) - \nabla_{\mathbf{r}'}\gamma(\mathbf{r}',\mathbf{r})] \\ &= \frac{\hbar}{2im_e}\sum_{i}^{\mathrm{NO}} n_i \left[\lambda_i^*(\mathbf{r}')\nabla_{\mathbf{r}}\lambda_i(\mathbf{r}) - \nabla_{\mathbf{r}'}\lambda_i^*(\mathbf{r}')\lambda_i(\mathbf{r})\right], \end{aligned} \tag{3.10}$$

where $\nabla_{\mathbf{r}}$ and $\nabla_{\mathbf{r}'}$ are the nabla with respect to $\mathbf{r}$ and $\mathbf{r}'$, respectively, and $\{\lambda_i\}$ are the natural orbitals with real-valued occupation numbers n_i. Since our nonadiabatically time-propagated electronic wavefunctions attained as the solutions of Eq. (3.2) are complex-valued, so are the resultant natural orbitals. As seen from Eq. (3.9), only complex-valued wave functions can give non-zero flux. Indeed, stationary-state electronic wavefunctions like most of the eigenfunctions of the electronic Hamiltonian $\hat{H}^{(el)}$ are real-valued, and thereby electron flux given by them are identically zero everywhere. This is simply because there is no directionality both in space and time in those stationary waves. Therefore appearance of nonzero flux, irrespective of the sign, indicates the breakdown of the stationarity, which suggests that the waves involved begin to proceed ahead to a certain direction in space-time. (See refs. [21–26] for applications of electron flux in chemical dynamics.) Consequently, integration of Eq. (3.8) gives how the electronic charge redistributes in time. This is not an easy task though, partly because the flux itself fluctuates pretty much both in time and space [21–24]. However, in this paper, we just monitor the flux $\vec{j}(\mathbf{r},t)$ by directly calculating $\gamma(\mathbf{r}',\mathbf{r})$ from the time-dependent electron wavepackets, without resorting to the integration of Eq. (3.8), because qualitative monitoring of the symmetry breaking is the present purpose.

Incidentally the total flux arising from the dynamics of a molecule should preserve the total symmetry in the total space-time representation. For instance, the total flux that is consisted of both electronic and nuclear counterparts should appropriately reflect translational and/or rotational symmetries in total. However, the present work treats only the electronic flux at each nuclear configuration. Manz and his group have been studying such total electronic and nuclear flux [25,26].

Also, we should recall that the couplings among the electronic configurations can contribute to $\vec{j}(\mathbf{r},t)$ only if they can remain in $\gamma(\mathbf{r}',\mathbf{r})$. For instance, the coupling between double excited configurations and a doubly occupied ground state configuration do not make a contribution to $\vec{j}(\mathbf{r},t)$, although these combinations are known to need to represent the dynamical electron correlation.

3.1.4 Unpaired Electron Population Analysis

Another useful quantity to detect the change in electronic states in excited states is the unpaired electron density [27–30]. It is defined with the spin-free first order density matrix as

$$D(\mathbf{r}) = 2\gamma(r,r) - \int \gamma(\mathbf{r},\mathbf{r}')\gamma(\mathbf{r}',\mathbf{r})d\mathbf{r}'. \tag{3.11}$$

The physical meaning will appear more evident if we express the diagonal element of $D(\mathbf{r})$ with the natural orbitals $\{\lambda_i\}$ having occupation numbers n_i

$$D(\mathbf{r}) = \sum_{i}^{\mathrm{NO}} n_i(2-n_i)\lambda_i^*(\mathbf{r})\lambda_i(\mathbf{r}). \tag{3.12}$$

As seen in Eq. (3.12), phenomena dominated by doubly occupied natural orbitals, such as concerted reactions, are not featured by large values of $D(\mathbf{r})$. On the other hand, nonadiabatic transitions and double excitation due to electron correlation will result in large $D(\mathbf{r})$ values, with the components of $n_i = 1$ giving the largest.

3.2 Integrals Calculating of Coupling Term

As mentioned, to put the above theory into practice at *ab initio* level, there are several technical problems have to be ironed out. One of them is to calculate the nuclear derivative coupling term.

By using one-electron coupling constant, expression of X_{IJ}^k can reduce from CSF bases to MO bases. After a series of derivation (detailed derivations of this section refer to Appendix A) it becomes

$$X_{IJ}^k = \sum_{ij}^{MO} a_{ij}^{IJ}(U_{ij}^k + S_{ij}^{kR}). \tag{3.13}$$

a_{ij}^{IJ} is the one-electron coupling constant with the form as

$$a_{ij}^{IJ} = \langle\Phi_I|\hat{a}_i^\dagger\hat{a}_j|\Phi_J\rangle, \tag{3.14}$$

where $\hat{a}_i^\dagger$ and $\hat{a}_j$ are creation and annihilation operators for molecular orbitals ϕ_i and ϕ_j, respectively.

U_{ij}^k is defined from nuclear derivatives of MO coefficients as

$$\frac{\partial c_\mu^i}{\partial k} = \sum_{m}^{MO} c_\mu^m U_{mi}^k. \tag{3.15}$$

And S_{ij}^{kR} is defined as

$$\begin{aligned} S_{ij}^{kR} &\equiv \sum_{\mu\nu}^{AO} c_\mu^i c_\nu^j S_{\mu\nu}^{kR} \\ &= \sum_{\mu\nu}^{AO} c_\mu^i c_\nu^j \langle\chi_\mu|\frac{\partial\chi_\nu}{\partial R_k}\rangle, \end{aligned} \tag{3.16}$$

where $\{\chi_\mu\}$ are AO bases used to form MO by linear combinations. The way to obtain them are introduced in the following sections based on GAMESS package.

3.2.1 Prepare One-electron Coupling Constants a_{ij}^{IJ}

By the definition of a_{ij}^{IJ}, some properties about it can be easily deduced. Such as

1. $a_{ij}^{IJ} = a_{ji}^{JI}$

2. If $a_{ij}^{IJ} \neq a_{ji}^{IJ}$, then at least one of them is zero.

3. For the following three situations, a_{ij}^{IJ} can be known directly:

   - if $i = j$, $I \neq J$, then $a_{ij}^{IJ} = 0$
   - if $i \neq j$, $I = J$, then $a_{ij}^{IJ} = 0$
   - if $i = j$, $I = J$, then $a_{ij}^{IJ} = 1$

4. For $i \neq j$, $I \neq J$, there are four situations:

   (a) $i > j$, $I > J$

   (b) $i < j$, $I > J$

   (c) $i > j$, $I < J$

   (d) $i < j$, $I < J$

   Since $a_{ij}^{IJ} = a_{ji}^{JI}$, only one pair of (a) and (b) or (c) and (d) are needed.

Firstly let us prepare (c) and (d). GAMESS has prepared a_{ij}^{IJ} in $I < J$ orders when calculate energy gradient. However, since the density matrix calculation need only picking up non-zero a_{ij}^{IJ}, so GAMESS saves data just in ij order without knowing $i < j$ or $i > j$. So according to property 2, we can judge the relation and then make anther part zero . Once obtained (c) and (d), (a) and (b) are known immediately. And the rest part can been determinate by property 3. Thus all of the a_{ij}^{IJ} can be obtained.

3.2.2 Prepare the Skeleton Integral S_{ij}^{kR}

GAMESS has prepared electron coordinate derivative coupling in AO basis sets, namely $\langle\chi_\mu|\partial_r\chi_\nu\rangle$. Since the one-center Gaussian function $\chi_\mu(r - R_k)$ has the relation of

$$\langle\chi_\mu|\frac{\partial\chi_\nu(r-R_k)}{\partial R_l}\rangle = -\langle\chi_\mu|\frac{\partial\chi_\nu(r-R_k)}{\partial r}\rangle\delta_{kl}, \tag{3.17}$$

So $\langle\chi_\mu|\partial_k\chi_\nu\rangle$ can be obtained by this relation. And then multiply MO coefficients to obtain S_{ij}^{kR}. δ_{kl} is Kronecker delta function.

Besides S_{ij}^{kR}, there are the other two integrals S_{ij}^{kL} and S_{ij}^{k} are needed for calculating X_{IJ}. They are defined by

$$S_{ij}^{kL} = \sum_{\mu\nu}^{MO} c_\mu^i c_\nu^j \langle\frac{\partial\chi_\mu}{\partial R_k}|\chi_\nu\rangle \tag{3.18}$$

and

$$\begin{aligned} S_{ij}^{k} &= \sum_{\mu\nu}^{MO} c_\mu^i c_\nu^j \frac{\partial\langle\chi_\mu|\chi_\nu\rangle}{\partial R_k} \\ &= S_{ij}^{kL} + S_{ij}^{kR}. \end{aligned} \tag{3.19}$$

S_{ij}^{k} are also denoted as S_{ij}^{a} below. Notice that S_{ij}^{kL} and S_{ij}^{kR} has the relation of

$$S_{ij}^{kR} = S_{ji}^{kL}. \tag{3.20}$$

So S_{ij}^{kL} and S_{ij}^{k} can be known once S_{ij}^{kR} obtained.

3.2.3 Prepare U Matrix U_{ij}^{k}

Determining U matrix needs solving CPHF equation [31–33], which comes from the nuclear derivative of Fock matrix

$$\frac{\partial F_{ij}}{\partial a} = -(\epsilon_j - \epsilon_i)U_{ij}^{a} + \sum_{k}^{virt}\sum_{l}^{occ} U_{kl}^{a} A_{ij,kl} + B_{0,ij}^{a}. \tag{3.21}$$

Relative definitions are as follows,

$$A_{ij,kl} = 4(ij|kl) - (ik|jl) - (il|jk), \tag{3.22}$$

$$B_{0,ij}^{a} = F_{ij}^{a} - S_{ij}^{a}\epsilon_j - \sum_{k}^{occ}\sum_{l}^{occ} S_{kl}^{a}\{2(ij|kl) - (ik|jl)\}, \tag{3.23}$$

$$S_{ij}^{a} = \sum_{\mu\nu}^{AO} c_{\mu}^{i} c_{\nu}^{j} \frac{\partial S_{\mu\nu}}{\partial a}, \tag{3.24}$$

$$F_{ij}^{a} = h_{ij}^{a} + \sum_{k}^{d.o.}\{2(ij|kk)^{a} - (ik|jk)^{a}\}, \tag{3.25}$$

$$h_{ij}^{a} = \sum_{\mu\nu}^{AO} c_{\mu}^{i} c_{\nu}^{j} \frac{\partial h_{\mu\nu}}{\partial a}, \tag{3.26}$$

$$(ij|kl)^{a} = \sum_{\mu\nu\rho\sigma}^{AO} c_{\mu}^{i} c_{\nu}^{j} c_{\rho}^{k} c_{\sigma}^{l} \frac{\partial(\mu\nu|\rho\sigma)}{\partial a}. \tag{3.27}$$

The superscript 'a' implies skeleton derivative without derivatives of MO coefficients.

Due to the properties of **U** matrix, it is convenient to divide it into four parts such as

1. $i \in occ, j \in occ$
2. $i \in virt, j \in virt$
3. $i \in occ, j \in virt$
4. $i \in virt, j \in occ$

For situation 4, Eq.(3.21) can be written as

$$(\epsilon_j - \epsilon_i)U_{ij}^{a} - \sum_{k}^{virt}\sum_{l}^{occ} U_{kl}^{a} A_{ij,kl} = B_{0,ij}^{a} \qquad (i \in virt, \quad j \in occ) \tag{3.28}$$

or a more compactly form as

$$\sum_{k}^{virt}\sum_{l}^{occ} U_{kl}^{a} C_{ij,kl} = B_{0,ij}^{a} \qquad (i \in virt, \quad j \in occ), \tag{3.29}$$

wherein

$$C_{ij,kl} = [(\epsilon_j - \epsilon_i)\delta_{ik}\delta_{jl} - A_{ij,kl}]. \tag{3.30}$$

So it becomes a matrix problem of

$$\mathbf{CU} = \mathbf{B} \tag{3.31}$$

wherein **C** is [ij, kl] array while **B** and **U** are [ij] (or [kl]) array. Notice that here **U** only includes the elements belong to situation 4. Since GAMESS has prepared **C** and **B** so that **U** can be solved by

$$\mathbf{U} = \mathbf{C^{-1}B}. \tag{3.32}$$

Once the subspace ($i \in virt, j \in occ$) of **U** has been determined, use the relation of

$$U^a_{ij} + U^a_{ji} + S^a_{ij} = 0 \tag{3.33}$$

situation 3 ($i \in occ, j \in virt$) can be obtained easily. At last, use another important relation of

$$U^a_{ij} = -\frac{1}{2}S^a_{ij}, \quad (i, j \in occ \quad \text{or} \quad i, j \in vir), \tag{3.34}$$

subspace of **U** for situation 1 and 2 can be also determined.

3.3 Unique-Continuity of Molecular Orbitals

Another problem is to ensure the unique-continuity of MO. To be bases to construct CSF, MOs are generated by SCF procedure at current nuclear configuration independently. So the choosing of the phase factor is arbitrary. Especially at the degenerated point, the MO order may be exchanged before and after the nuclear dynamics step, and CSF will lose original feature and result in failed dynamics at all.

3.3.1 Theoretical Method

The following method proposed by Yonehara et al. aims at settling this problem [34]. Firstly, the overlap matrix

$$S_{ij} = \langle \phi_i(t - \Delta t) | \phi_j(t) \rangle \tag{3.35}$$

is introduced. The closer to δ_{ij} it is, the better orbital uniformity along nuclear path. Assume $|\phi_i(t - \Delta t)\rangle$ has been known by last step calculation, $|\phi_j(t)\rangle$ can be expressed by linear combination of trial MOs

$$|\phi_j(t)\rangle = \sum_k^{\mathrm{MO}} C_{kj} |\tilde{\phi}_k(t)\rangle, \tag{3.36}$$

where $|\tilde{\phi}_k(t)\rangle$ are from current SCF step.

To determine C_{kj}, a new overlap matrix

$$O_{ik} = \langle \phi_i(t - \Delta t) | \tilde{\phi}_k(t) \rangle \tag{3.37}$$

is formed. Notice the relation

$$S_{ij} = \sum_{k}^{\mathrm{MO}} O_{ik} C_{kj}. \tag{3.38}$$

To get qualified S_{ij}, the formal solution of C_{kj} is

$$\mathrm{C} = \mathrm{O}^{-1}. \tag{3.39}$$

But such a C can not be used directly to form $|\phi_j(t)\rangle$ since it is not exactly orthogonal that may break the orthonormality of $|\tilde{\phi}_k(t)\rangle$. One way to preserve the orthonormality is to make O a orthogonal matrix before executing Eq.(3.39), e.g., by Gram-Schmidt algorithm to do O= QR, and C is given by

$$\mathrm{C} = \mathrm{Q}^{-1} = \mathrm{Q}^{\mathrm{T}}. \tag{3.40}$$

Meanwhile, for numerical stability, it is not necessary to put the whole space of O into Gram-Schmidt procedure as it is once formed. Only subspaces with strong mixing need rotation.

Finally, once $|\phi_j(t)\rangle$ is obtained, corresponding orbital energy is given by

$$\varepsilon_j(t) = \sum_{k}^{\mathrm{MO}} C_{kj}^2 \tilde{\varepsilon}_k(t), \tag{3.41}$$

wherein $\tilde{\varepsilon}_k(t)$ is primary orbital energy of $|\tilde{\phi}_k(t)\rangle$.

3.3.2 Numerical Illustration

By the above procedures, we study a collinear collision reaction between B^+ and H_2 to show the necessity for MO continuity. Set the initial nuclear distances as $R_{\mathrm{B-H}} = 4.0$ Å and $R_{\mathrm{H-H}} = 0.8$ Å and start from the second exicted state by CIS/STO-3G method, and give relative kinetic energy of 1.57 eV to the system; the results are shown as below.

Since our foucs is not on the reaction but is on the MO before and after the correction, so we track the MO by plotting its eigenvector and eigenvalue. Concretely, the MO coefficients in the atomic orbital bases are plotted as in Fig. 3.2. It can be seen clearly that if without correction, SCF procedure at isolate nuclear configurations cannot describe the dynamics. To understand it in a more straight way, the energies of the pairs of mixing MOs are shown as in Fig. 3.3. It can be seen that if without correction, the MOs lose their charactistics and are not qualified to construct the CSF any more.

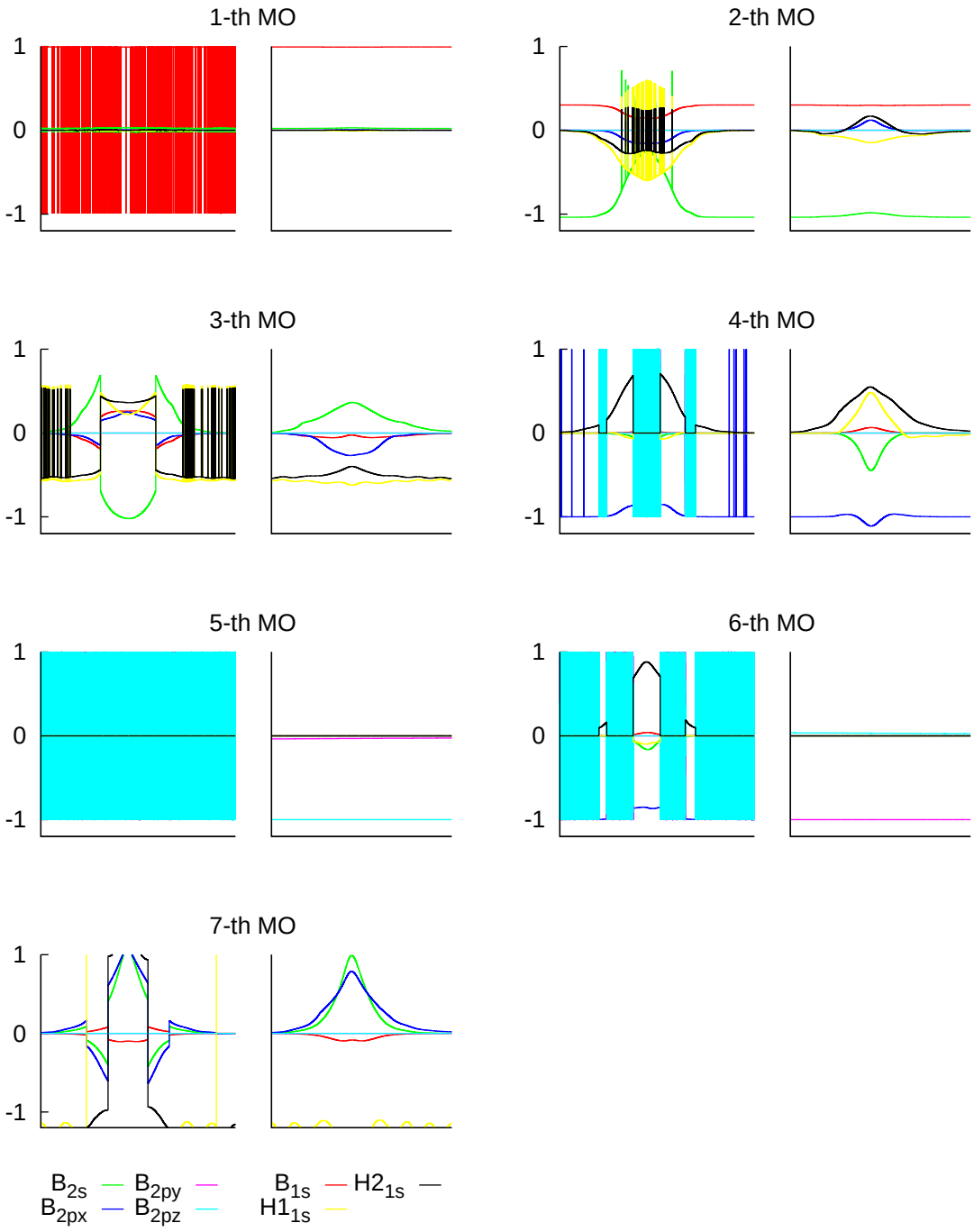

FIG. 3.2: MO coefficients before (the left ones) and after (the right ones) uniform correction of the B^++H_2 collision reaction. Abscissa is time till 50 fs.

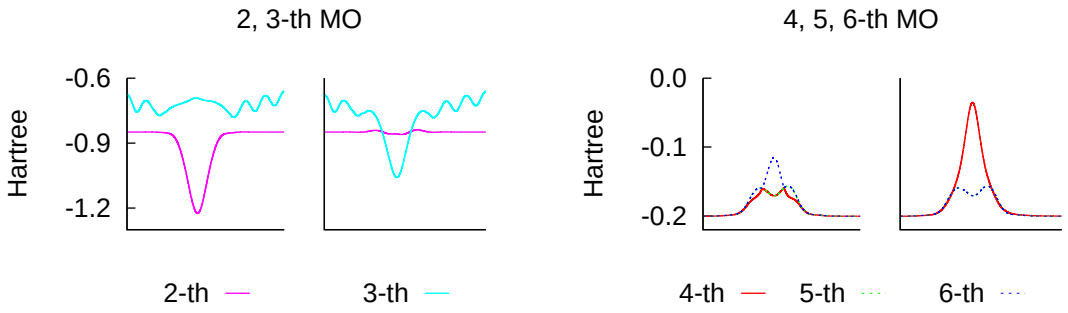

FIG. 3.3: The energies before (the left ones) and after (the right ones) uniform correction of selected mixing MO pairs of the B^++H_2 collision reaction.. Abscissa is time till 50 fs.

Reference

[1] T. Yonehara, and K. Takatsuka, J. Chem. Phys. 128 (2008) 154104.

[2] K. Takatsuka, J. Phys. Chem. A 111 (2007) 10196.

[3] Y. Arasaki, K. Takatsuka, K. Wang, and V. McKoy, Phys. Rev. Lett. 90 (2003) 248303.

[4] Y. Arasaki, K. Takatsuka, K. Wang, and V. McKoy, J. Chem. Phys. 119 (2003) 7913.

[5] Y. Arasaki, K. Takatsuka, K. Wang, and V. McKoy, J. Chem. Phys. 132 (2010) 124307.

[6] Y. Arasaki, K. Wang, and V. McKoy, K. Takatsuka, Phys. Chem. Chem. Phys. 13 (2011) 8681.

[7] P. M. Kraus, Y. Arasaki, J. B. Bertrand, S. Patchkovskii, P. B. Corkum, D. M. Villeneuve, K. Takatsuka, and H. J. Wöner, Phys. Rev. A 85 (2012) 043409.

[8] K. Takatsuka, T. Yonehara, K. Hanasaki, and Y. Arasaki, Chemical Theory beyond the Born-Oppenheimer Paradigm (World Scientific, Singpore, 2015).

[9] T. Yonehara, and K. Takatsuka, J. Chem. Phys. 129 (2008) 134109.

[10] T. Yonehara and K. Takatsuka, J. Phys. Chem. A 117 (2013) 8599.

[11] K. Yamamoto and K. Takatsuka, J. Chem. Phys. 140 (2014) 124111.

[12] H.-D. Meyer and W. H. Miller, J. Chem. Phys. 70 (1979) 3214.

[13] D. A. Micha, J. Chem. Phys. 78 (1983) 7138.

[14] A. García-vela, R. B. Gerber, and D. G. lmre, J. Chem. Phys. 97 (1992) 7242.

[15] W. H. Miller, Faraday Discuss. 110 (1998) 1.

[16] M. D. Hack, A. W. Jasper, Y. L. Volbuev, D. W. Schwenke and D. G. Truhlar, J. Phys. Chem. A 104 (2000) 217.

[17] M. Amano and K. Takatsuka, J. Chem. Phys. 122 (2005) 084113.

[18] T. Yonehara, and K. Takatsuka, J. Chem. Phys. 132 (2010) 244102.

[19] T. Yonehara, and K. Takatsuka, J. Chem. Phys. 137 (2012) 22A520.

[20] L. I. Schiff, Quantum Mechanics (McGraw-Hill: New York 1968).

[21] K. Nagashima, and K. Takatsuka, J. Phys. Chem. A 113 (2009) 15240.

[22] K. Nagashima, and K. Takatsuka, J. Phys. Chem. A 116 (2012) 11167.

[23] M. Okuyama and K. Takatsuka, Chem. Phys. Lett. 476 (2009) 109.

[24] M. Okuyama and K. Takatsuka, Bull. Chem. Soc. Jpn. 85 (2012) 217.

[25] I. Barth, H.-C. Hege, H. Ikeda, A. Kenfack, M. Koppitz, J. Manz, F. Marquardt, and G. K. Paramonov, Chem. Phys. Lett. 481 (2009) 118.

[26] J. Manz, J. F. Peréz-Torres, and Y. Yang, J. Phys. Chem. A 118 (2014) 8411.

[27] K. Takatsuka, T. Fueno, and K. Yamaguchi, Theoret. Chim. Acta 48 (1978) 175.

[28] K. Takatsuka and T. Fueno, J. Chem. Phys. 69 (1978) 661.

[29] V. N. Staroverov, and E. R. Davidson, J. Am. Chem. Soc. 122 (2000) 186.

[30] V. N. Staroverov, and E. R. Davidson, Chem. Phys. Lett. 330 (2000) 161.

[31] R. M. Stevens, R. M. Pitzer, and W. N. Lipscomb, J. Chem. Phys. 38 (1963) 550.

[32] J. Gerratt, and I. M. Mills, J. Chem. Phys. 49 (1968) 1719.

[33] Y. Yamaguchi, Y. Osamura, J. D. Goddard, and H. F. Schaefer, A New Dimension to Quantum Chemistry: Analytic Derivative Methods in Ab Initio Molecular Electronic Structure Theory (Oxford, New York 1994).

[34] T. Yonehara, K. Hanasaki, and K. Takatsuka, Chem. Rev. 112 (2012) 499.

Chapter 4

Symmetry Breaking Dynamics of the Low-lying Excited States of B_4

This chapter are numerical resutls. We first see the ground state to get a global insight of the PES, and then choose one excited state to give a detailed analysis while other two excited states are discussed in a similar way.

Since the present work aims at tracking nonadiabatic dynamics of symmetry breaking rather than accurate energy prediction, STO-3G basis set is used to perform most of the calculations. Configuration interaction is performed in the level of single and double excitations [1, 2] with four core orbitals being frozen. 1891 CSFs are generated by GUGA (Graphical Unitary Group Approach) which has been packaged in GAMESS [3] (2013/05/01 version). These CSF are also applied in the study of electron wavepacket dynamics.

Equations (3.2) and (3.6) should be solved simultaneously. However, due to different time scales of electrons and nuclei, integrators and intervals can be chosen independently. The fourth order Runge-Kutta method is used as integrator to propagate Eq. (3.2), and integration interval is set to be 0.05 attoseconds. To save computational cost, in contrast to multistep Runge-Kutta, multi-value method is used to propagate nuclear phase space. So the third and the fourth order Taylor series of $\dot{R}_k$ and R_k are calculated respectively at each step. Derivatives higher than the second order are obtained approximately by the corresponding difference equations. Time interval is set to be 2.5 attoseconds, which is 50 times longer that of electronic dynamics. At these settings, total energy is generally conserved at the level of 10^{-8} hartrees except downgrading to 10^{-6} level in passing through the "crossing" areas.

4.1 Ground State: ^1A_g

4.1.1 SCF-MO

HFSCF-MOs at the stationary structure (D_{2h}, $\theta = 78°$, bond length is 1.501 Å) are shown in Fig. 4.1. Comparison with Fig. 2.8 shows that the nodal structure of the molecular orbitals generated in these two sets of molecular orbitals are essentially same, and thus it turns out that the Hückel orbitals are very useful to understand the molecular symmetry intuitively and graphically. Other points we notice with respect to the relevant MO calculations in the literature are: (1) Unoccupied $2s$-based orbital noticed by Wang et al. [4] is actually the lowest *sp* anti-bonding orbital in Hückel-MO. (2) The $2a_g$ bonding orbital surprisingly becomes unoccupied according to extended Hückel calculations [5]. (3) Hybridization inevitably mixes a little p_r and p_t by any SCF procedure. But for cyclic-B_4, it is safe to say that p_π, p_r 4c-2e bonds and $2s$-p_t hybridization are robust.

Although the first singlet excited state is claimed to be the single occupancy of $2b_{2u}$, the excitation to $3a_g$ is also competitive. The two are just LUMO+1 and LUMO here and evolve closely in the excited dynamics.

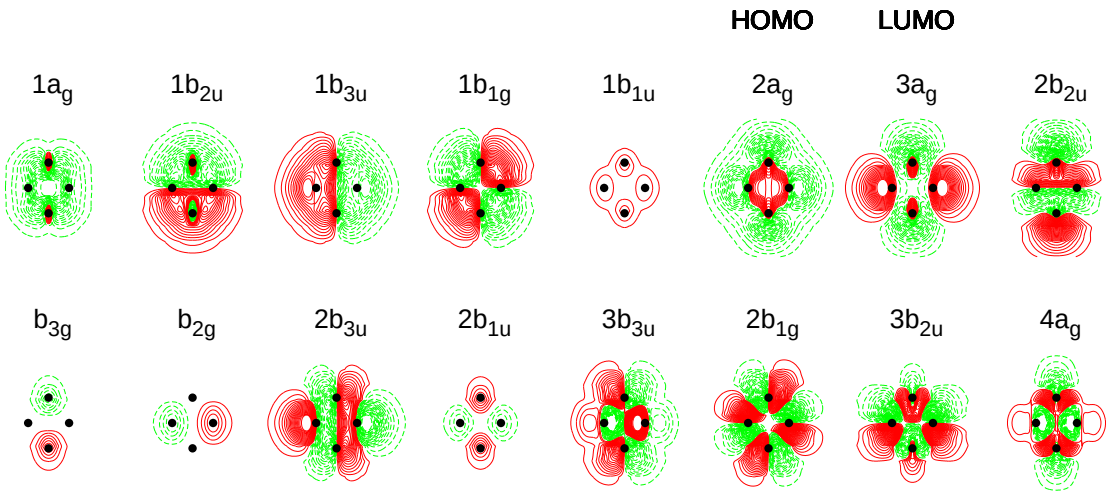

FIG. 4.1: RHF/STO-3G predicted MO lies in the xy sections with $z = 0.1$ bohr. Black dots indicate nuclei.

4.1.2 Adiabatic Potential Energy Surfaces

As known, the D_{4h} structure is in fact a saddle point with one weak imaginary frequency along $\omega_1(A_g)$ mode to connect the two D_{2h} minima. The two optimized structures ($\theta = 78°$ or $102°$) identified in the present calculations are in the reasonably correct range as compared with other high accuracy methods [6–8]. The barrier is so tiny (0.025 eV) that $1.5\times h\nu_1$ (0.06 eV), with ν_1

being the vibrational frequency of $\omega_1(A_g)$ mode, is enough to cause *dsd* rearrangement to occur at the ground state (see Fig. 4.2). Besides, bond lengths of edges are well preserved around 1.5 Å during the reaction coordinate θ. Also, the charges on the atoms is almost invariant (at most 0.04) during *dsd*. The so-called bond order analysis in the Mulliken overlap population formalism gives about 0.9 population on edge, but merely weak bonding or anti-bonding exists between diagonals.

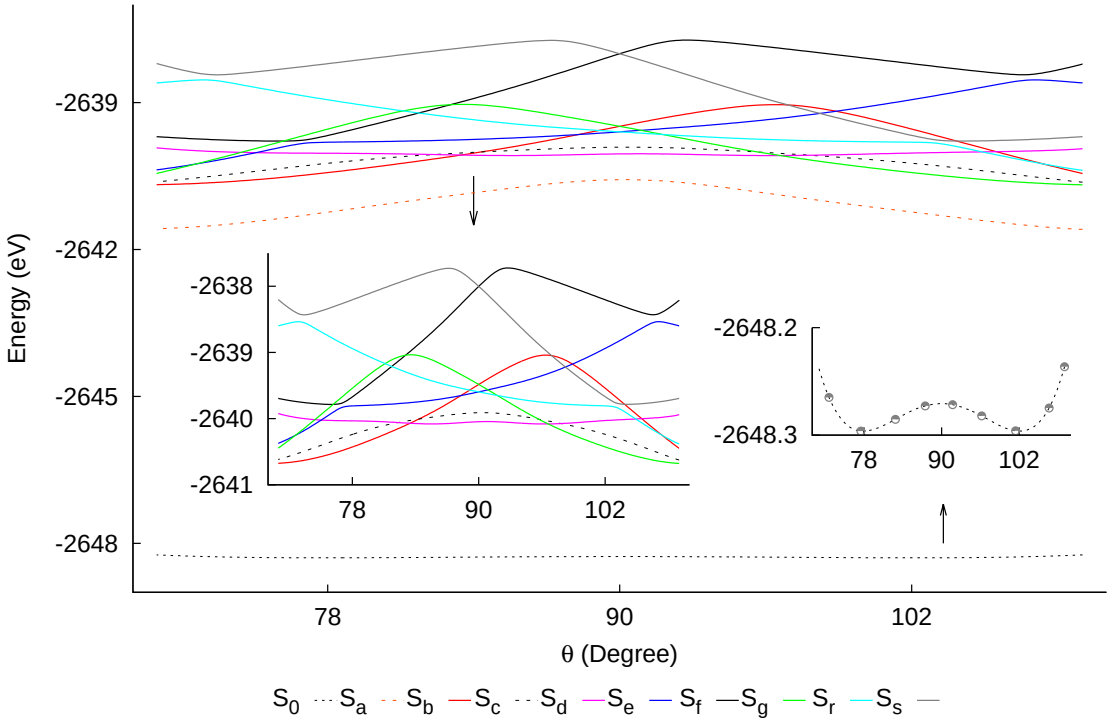

FIG. 4.2: Potential energy surfaces of the low-lying excited states as deformed along the *dsd* $\omega_1(A_g)$ mode. These curves represent the one-dimensional change along θ of the states listed in Table 4.1.

The bond order analysis reduced on six occupied valence orbitals shows that the bonding *sp* and p_π orbitals form the skeleton of cyclic-B_4 (Fig. 4.3). At the diagonal (central) area, although gross bond order is nearly zero, there is in fact comparative bonding or anti-bonding area in *sp* bonding orbitals, which mutually cancel out. The necessity of employing a and b in Hückel theory is suggested here again. The orbital $2a_g$ coming from the p_r set makes only a small contribution to the bonding, and for this reason loss of electrons from this orbital is still kept stable as seen later.

The most important information in Fig. 4.2 relevant to the present dynamics is the curve crossing feature among the excited states, which is magnified in the middle part of the figure. The characterization of the excited states involved is summarized in Table 4.1. This table contains main electronic configurations, their belonging irreducible representation of D_{2h}, oscillator strength and excitation energy. All of these quantities have been calculated at the geometry of the ground state minimum ($\theta = 78°$). The individual excitation energies are not necessarily meaningful but suggest

the relative height of the states. The potential curve crossing feature in Fig. 4.2 is compared with that expected by the Hückel calculations, Fig. 2.9(b). Except for one avoided crossing between two B_{3g} states, namely S_e and S_f, all the rest crossings indicate symmetry-allowed conical intersections. On passing through those conical intersections, nonadiabatic interactions induces symmetry breaking from D_{2h} by the mixing among them.

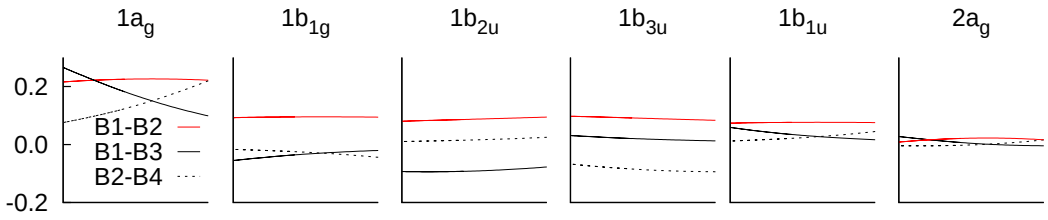

FIG. 4.3: Standard bond order of B_4 reducing on dominant occupied natural orbitals.

Table 4.1: CISD/RHF/STO-3G predicted nine singlet excited states of *rhombo*-B_4.

	Dominant Configuration[a]	CSF Coefficient	Symmetry	Oscillator Strength	Excitation Energy(eV)
S_a	$\Phi_{2a_g\to 3a_g}\equiv\Phi_a$	0.772	A_g	-	7.04
S_b	$\Phi_{2a_g\to 2b_{2u}}\equiv\Phi_b$	0.762	B_{2u}	0.121390, y-allowed	7.86
S_c	$\Phi_{1b_{1g}\to 3a_g}\equiv\Phi_c$	0.897	B_{1g}	-	8.05
S_d	$\Phi_{1b_{1u}\to 3a_g}\equiv\Phi_d$	0.917	B_{1u}	0.000518, z-allowed	8.25
S_e	$\Phi_{2a_g\to b_{3g}}\equiv\Phi_e$	0.893	B_{3g}	-	8.49
S_f	$\Phi_{1b_{1u}\to 2b_{2u}}\equiv\Phi_f$	0.875	B_{3g}	-	8.61
S_g	$\Phi_{1b_{1g}\to 2b_{2u}}\equiv\Phi_g$	0.880	B_{3u}	0.021416, x-allowed	8.74
S_r	$\Phi_{2a_g\to b_{2g}}\equiv\Phi_r$	0.905	B_{2g}	-	9.36
S_s	$\Phi_{1b_{1g}\to b_{3g}}\equiv\Phi_s$	0.932	B_{2g}	-	10.09

[a] "$\to$" denotes single excitation

4.2 Excited State: $^1B_{2u}$

4.2.1 Distincts of Different Point Groups

We here show a case study of symmetry breaking dynamics by tracking a SET path starting from the excited state, which we call S_b, the main configuration of which is single excitation from $2a_g$ orbital to $2b_{2u}$ one as listed in Table 4.1. This state has relatively large oscillator strength in y-direction for the excitation from the ground state. Through such an illustrative case study, we hereby investigate how the electronic states of different symmetry can mix through nonadiabatic interactions and how

the resultant states may behave vibrationally and electronically.

Since S_b has two singly occupied orbitals $2b_{2u}$ and $2a_g$, once being excited, B_4 spontaneously vibrates along the $\omega_1(A_g)$ direction with no initial nuclear momentum. To demonstrate the dynamical change by the electronic state mixing as much as possible, we do not provide much energy to vibrational modes, actually only zero point energy along the two A_g modes is assigned. Nevertheless, the electronic state mixing develops in a consecutive manner.

In view of the complexity of those nonadiabatic dynamics, the following materials are used to make the processes easier to be tracked: (1) Time section tables (Table 4.2). The studied time scale, about 400 fs, is divided into several sections in light of the change of molecular symmetry. Dominant configurations in our interested states are summarized in this table. Orbital symmetries may change in different time sections but names in Fig. 4.1 are continuously adopted as new symmetry labeled. (2) Time variation of the concerned physical quantities, e.g. nuclear distances and CSF population, etc. (Fig. 4.4). Nuclear velocity is certainly an important factor for the kinematic coupling dynamics but it is not attached because essential information can be easily guessed in the nuclear distance panel.

4.2.2 Dynamics of Symmetry Breaking

Giving zero point energy to $\omega_1(A_g)$ mode (0.02 eV), we let S_b start its dynamics, as shown in Table 4.2 and Fig. 4.4. We first overview the geometrical change by taking a close look at the nuclear distance panel, Fig. 4.4(a) and Table 4.2. Although initial momentum is given towards the directions to the square, a complete direction reversal happens rapidly. Occupancy of $2b_{2u}$ orbital strongly drives rhombic B_4 to be narrower (smaller θ) and even if much more initial kinetic energy be assigned, and *dsd* is hard to occur. If excitation to $2b_{2u}$ is replaced with that to $2b_{3u}$, *dsd* should be much easier. Thus the vibration is limited in the primary *diamond* section, simply called half-period $\omega_1(A_g)$ vibration. Such a narrower structure caused by $2b_{2u}$ was also observed through bond shortening from B_4 to ${B_4}^{-1}$ [8]. The regular D_{2h} point group is just retained only up to 38 fs before the $\sigma(xy)$ symmetry element begins to be slightly destroyed. Such a quasi-D_{2h} state lasts about 20 fs before z-symmetry is markedly broken and the $\omega_2(B_{1u})$ out-of-plane vibration is realized due to the nonadiabatic interaction. Furthermore, upon entering $C_{2v}(z)$ section, the $\sigma(xz)$ continuously begins to lose at about 126 fs, leading to a quasi-$C_{2v}(z)$ state. At this time the quasi-state exists just within 5 fs and the y-symmetry is rapidly broken down. $\omega_5(B_{2u})$ becomes thus involved. The last symmetry element $\sigma(yz)$, which is related to $\omega_3(B_{3u})$ or $\omega_6(B_{1g})$, begins to be lost from 215 fs. Until the x-symmetry is finally crashed, the quasi-$C_s(yz)$ state actually survives almost 59 fs.

Such a series of dynamical change can be highlighted more vividly in terms of quantities to characterize electron dynamics, which will be studied below.

Table 4.2: Time sections of nonadiabatic dynamics starting from S_b.

S_b−I	0∼[38]∼62 fs[a] (D_{2h})
Configurations (B_{2u})	Φ_b, Φ_h, Φ_i, Φ_j
Orbitals	$1b_{1g}$, $1b_{1u}$, $2a_g$, $3a_g$, $2b_{2u}$, b_{3g}, $2b_{3u}$
Notes	$1b_{1u}$∼$2a_g$ begins to break z-symmetry after 38 fs.
S_b−II	62∼[126]∼131 fs ($C_{2v}(z)$[b])
Configurations (B_2)	Φ_b, Φ_h, Φ_i, Φ_j, Φ_f
Orbitals	$1b_{1g}(a_2)$, $1b_{1u}(a_1)$, $2a_g(a_1)$, $3a_g(a_1)$, $2b_{2u}(b_2)$, $b_{3g}(b_2)$, $2b_{3u}(b_1)$
Notes	$1b_{1u}(a_1)$∼$2a_g(a_1)$ breaks z-symmetry at all after 62 fs. $3a_g(a_1)$∼$2b_{2u}(b_2)$ begins to break y-symmetry after 126 fs.
S_b−III	131∼[215]∼273 fs ($C_s(yz)$[c])
Configurations ($A^{'}$)	Φ_b, Φ_h, Φ_i, Φ_j, Φ_f, Φ_d, Φ_a
Orbitals	$1b_{1g}(a^{''})$, $1b_{1u}(a^{'})$, $2a_g(a^{'})$, $3a_g(a^{'})$, $2b_{2u}(a^{'})$, $b_{3g}(a^{'})$, $2b_{3u}(a^{''})$
Notes	$3a_g(a^{'})$∼$2b_{2u}(a^{'})$ breaks y-symmetry at all after 131 fs. $1b_{1g}(a^{''})$∼$2a_g(a^{'})$ begins to break x-symmetry after 215 fs.
S_b−IV	273∼400 fs (C_1)
Configurations (A)	Φ_b, Φ_h, Φ_i, Φ_j, Φ_f, Φ_d, Φ_a, Φ_g, Φ_q
Orbitals	$1b_{1g}(a)$, $1b_{1u}(a)$, $2a_g(a)$, $3a_g(a)$, $2b_{2u}(a)$, $b_{3g}(a)$, $2b_{3u}(a)$
Notes	$1b_{1g}(a)$∼$2a_g(a)$ breaks x-symmetry at all after 273 fs.

[a] the second subsection means quasi-state (for the definition refer to the text)

[b] means C_2 lies in z-axis.

[c] means σ_h lies in yz-plane.

The electronic configurations in this table should be referred to Tabs. 4.1 and 4.3.

Table 4.3: Involved configurations in the present system[a]. Some of them are introduced for S_d and S_g discussions.

Φ_h	$2a_g$⇒$3a_g$, $2b_{2u}$	Φ_i	$1b_{1u}$→b_{3g}	Φ_j	$1b_{1g}$→$3a_g$
Φ_l	$1b_{1u}$, $2a_g$⇒$3a_g$	Φ_m	$1b_{1u}$, $2a_g$⇒$2b_{2u}$	Φ_n	$1b_{1u}$, $2a_g$⇒$3a_g$, $2b_{2u}$
Φ_o	$1b_{1g}$, $2a_g$⇒$3a_g$, $2b_{2u}$	Φ_p	$2a_g$→$2b_{3u}$	Φ_q	$1b_{1g}$→$2b_{3u}$

[a] "⇒"denotes double excitation

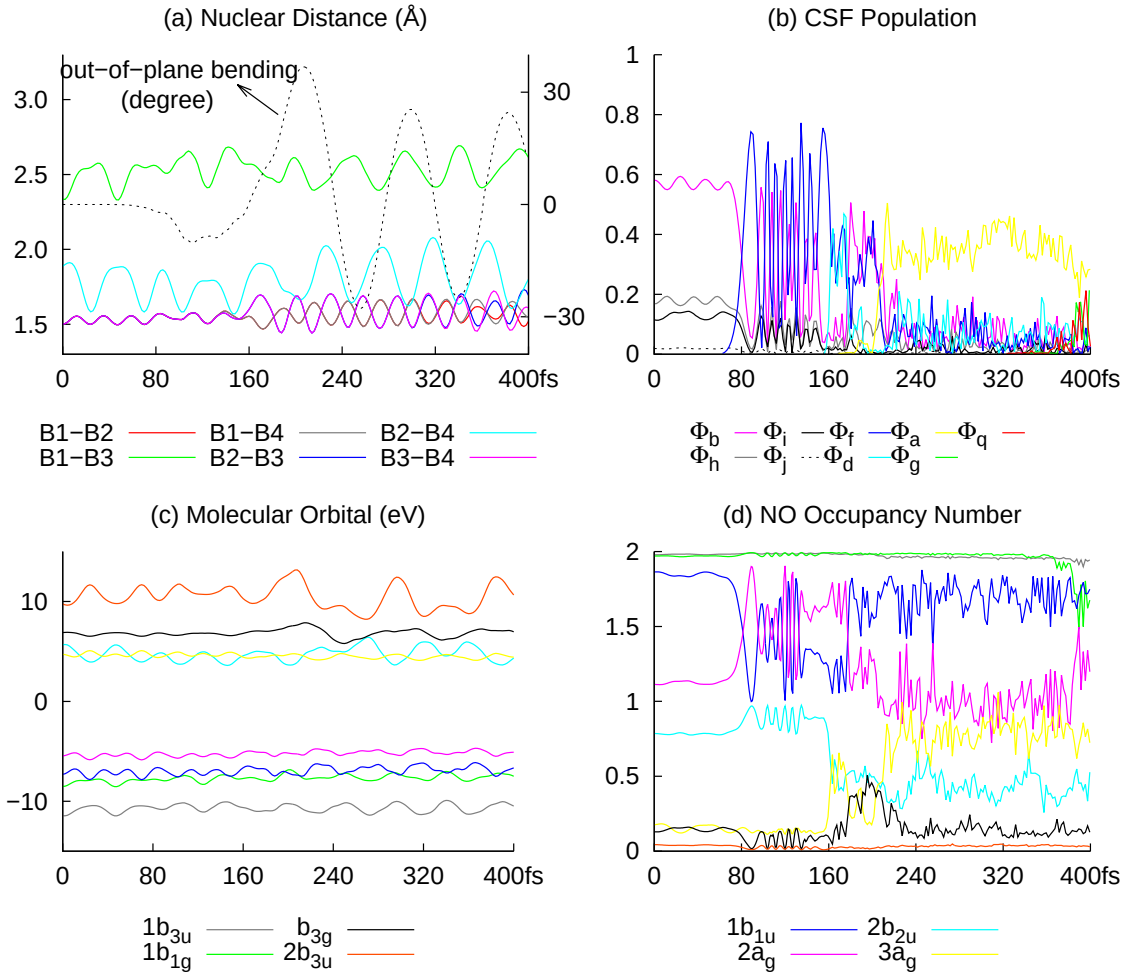

FIG. 4.4: Selected quantities along dynamics starting from S_b. Panels (c) and (d) share the same key labels.

4.2.3 Electron Flux Associated with Symmetry Breaking

We first see what happens in the electron flux induced by the nonadiabatic couplings. The first breaking z-symmetry directly indicates the existence of nonzero asymmetric z-vector electronic flux, simply called z-flux (without special information, all the flux discussed subsequently is asymmetric since symmetric flux does not affect the molecular point group). See Fig. 4.5 for the evolution of the electron flux. Among seven involved orbitals in the S_b-I time section, z-allowed electronic transitions are produced by the interactions $1b_{1u}$∼$2a_g$, $1b_{1u}$∼$3a_g$ and $2b_{2u}$∼b_{3g} ("∼"denotes orbital interaction). As suggested in Eq. (3.10), the flux due to, for instance $1b_{1u}$∼$2a_g$, arises from the density matrix $\gamma(\mathbf{r}', \mathbf{r})$ that contains $1b_{1u}$ and $2a_g$ symmetries. Recall that those $\gamma(\mathbf{r}', \mathbf{r})$ are resulted only from two different Slater determinants, which are composed of the same molecular orbitals except for only counterpart; one is $1b_{1u}$ orbital and the other $2a_g$ orbital. Thus the flux of $1b_{1u}$∼$2a_g$ is

likely generated mainly between an electronic configurations of excitation $1b_{1u}\rightarrow 2b_{2u}$ and $2a_g\rightarrow 2b_{2u}$. Likewise, the flux $1b_{1u}\sim 3a_g$ should come from the interaction between the ground configuration and $1b_{1u}\rightarrow 3a_g$. Also, $2b_{2u}\sim b_{3g}$ suggests the presence of interaction between the configurations of $2a_g\rightarrow 2b_{2u}$ and $2a_g\rightarrow b_{3g}$.

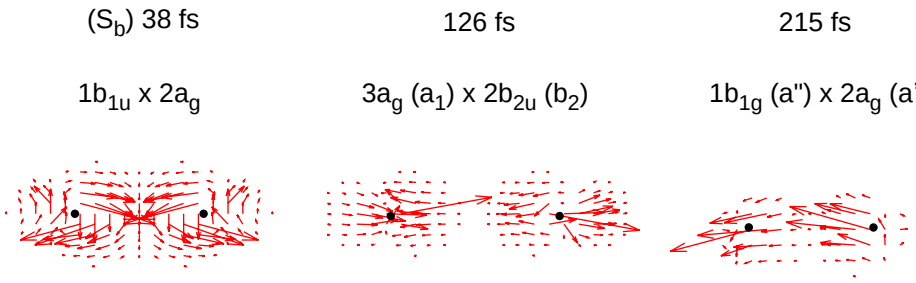

FIG. 4.5: Electron flux at selected time points. They are induced by the set of molecular orbitals indicated. Those at 38 fs and 215 fs are xz-section at $y = 0$ bohr, and 126 fs is yz-section at $x = 0$ bohr.

The more intense interaction happens, the more violent electronic flux is produced. At selected time point such as 38 fs, the largest z-vectors of the three orbital intersections induced flux reach 4.8×10^{-4}, 1.1×10^{-4} and 1.9×10^{-4}, respectively, in atomic units (the following data for flux just indicate the largest vectors in the discussed direction). It turns out that once z-symmetry begins to be a little destroyed, more symmetry-adapted configurations with respect to the degraded point group can be involved. Such as $\Phi_f(B_2)$ after 62 fs, which excites the population of $1b_{1u}(a_1)$ completely, makes a stronger interaction of $1b_{1u}(a_1)\sim 2a_g(a_1)$ become possible. Evidently, the above three values achieves 7.4×10^{-3}, 1.7×10^{-3}, 3.8×10^{-3} at 63 fs and are becoming larger. Thus the z-symmetry inevitably collapses.

The correlation between electron flux and state-mixing is summarized as follows: As shown above, the leading interaction for z-flux is $1b_{1u}\sim 2a_g$. Generally, flux favors interacting orbitals where virtual excitation happens readily [9], and the effective flux requires both concerned orbitals to participate the relevant configurations. In the S_b case, while $2a_g$ is singly occupied and $1b_{1u}$ is partly occupied at the beginning (see panel (d) in Fig. 4.4), the population of the latter orbital is much varied by $\Phi_f(B_2)$ subsequently. In addition, the partial occupation of b_{3g} suppresses the y-flux inducer $3a_g\sim 2b_{2u}$ to some extent by its own $2b_{2u}\sim b_{3g}$, which assists to break z-symmetry in the early stage. Despite of zero initial kinetic energy, $\omega_2(B_{1u})$ vibration is caused prior to other non-A_g modes, which is in fact a characteristic of S_b dynamics. Thus the physical (geometrical) propagation of electronic distribution due to nonadiabatic interactions manifests itself as the electron flux. Incidentally, z-allowed $1b_{3u}(b_1)\sim 2b_{3u}(b_1)$ as well as $2a_g(a_1)\sim 3a_g(a_1)$ induced z-flux are insignificant

to the magnitude of 10^{-5}.

Notice the crossing between $3a_g$ and $2b_{2u}$ at 35 fs and 60 fs (see panel (c) in Fig. 4.4), which is just before the above mentioned z-symmetry broken process. Even if $3a_g$∼$2b_{2u}$ interaction is not explicitly involved in the current time section, its significance has been coming in. In this way, the electron flux exhibits a sensitive reflection of the kinetic-coupled electronic dynamics.

Subsequently, by a chance of MO crossing point around 126 fs, $3a_g(a_1)$∼$2b_{2u}(b_2)$ induced y-flux just becomes activated (e.g. 5.0×10^{-4} at 126 fs). Since it is a strong interaction, y-symmetry is broken rapidly by y-flux. This is the origin of short-lived quasi-$C_{2v}(z)$. $\Phi_d(A^{'})$ and $\Phi_a(A^{'})$ appear after 155 fs and enhance further destruction of the y-symmetry, and thereby allow $\omega_5(B_{2u})$ to be involved.

In D_{2h} group, the only possible x-flux interaction is $1b_{3u}$∼$2a_g$. It comes into view at 215 fs (1.2×10^{-4}) as the interaction concerning $2a_g(a^{'})$ is released by $1b_{1u}(a^{'})$∼$2a_g(a^{'})$ to some extent (see panel (d) in Fig. 4.4). But $1b_{3u}(a^{''})$∼$2a_g(a^{'})$ itself is so weak and effective configurations with $1b_{3u}(a^{''})$ are always few. Instead, $1b_{1g}(a^{''})$∼$2a_g(a^{'})$ is a stronger interaction to induce the x-flux (e.g. 2.2×10^{-4} at 215 fs) in $C_s(yz)$ group. However, the relative configuration concerning $1b_{1g}(a'')$ of Φ_j (see Table 4.3) is energetically unfavorable. That is why the quasi-$C_s(yz)$ state lasts so long. Until $\Phi_g(A)$ and $\Phi_q(A)$ arise after 340 fs, interaction concerning $1b_{1g}(a)$ just becomes more apparent and $\omega_6(B_{1g})$ gets participated significantly.

The similar dynamics of electron flux develops, reflecting the further electronic state mixing. These nonadiabatic interactions last long without dissociation of B_4, which leads the electronic states to more and more complicated situation as time passes. However, the feature of nonadiabatic transitions through conical intersections and the resulting appearance of the electron flux is essentially similar to those described as above for the early stage dynamics.

4.2.4 Radical Characters

In recent synthesis chemistry, reactivity of compounds having σ- or π-boryl radicals is intensely studied in both theoretical and experimental aspects [10,11]. In excited state dynamics, we are particularly interested in the mixing between the σ- and π-states, which will be created by spontaneous breaking of spatial symmetry.

In Fig. 4.6 are shown snapshots of the three-dimensional distributions of the unpaired electron at three selected times: At 38 fs, molecular symmetry is the same as the initial one. As seen in the figure, the radicals (actually two radicals, 0.99 and 0.95 unpaired electrons belonging to $2a_g$ and $2b_{2u}$ orbitals, respectively) are widely distributed in the σ-plane, and interestingly they are delocalized on four boron atoms in the σ-plane. As z-symmetry is broken, the σ-π orthogonality is not preserved and one unpaired electron transfers from $2a_g(a_1)$ to $1b_{1u}(a_1)$ (e.g. at 126 fs). As a result, radicals are pushed to be localized mostly on the two diagonal pairs of atoms (B1 and B3),

and small components of the π radical are seen on B2 and B4. However, such clear π radicals do not remain long and indeed σ-π radical oscillation centered mainly on B2 and B4 atoms follows from 90 fs to 215 fs (see panel (d) of Fig. 4.4). Then, as y-symmetry has been broken, by a chance of $1b_{1g}(a'')\sim1b_{1u}(a')$ as well as $3a_g(a')\sim2b_{2u}(a')$ MO crossing points, simultaneously with a nuclear velocity minimum (see panel (a) of Fig. 4.4), where nonadiabatic flux becomes relatively apparent, the σ-σ flux is enhanced while σ-π flux decreases after 215 fs. After all $1b_{1u}(a')$ stops oscillation and ends with nearly double occupancy. Since the single occupied $2b_{2u}(a')$ is partly replaced by single occupied $3a_g(a')$, the σ radicals become more delocalized again.

Due to the initial conditions chosen here, the molecular shape of out-of-plane motion does not develop to a large extent, remaining more or less close to the planar structure. However, it is obviously inappropriate to track the unpaired electron density with the SET after when the wavepacket has well bifurcated due to nonadiabatic interactions. Path-branching dynamics will isolate the π-radical component more clearly.

4.2.5 Spectral Representation of the Electronic State Mixing

As above we have tracked the electronic state mixing due to a series of nonadiabatic interactions through conical intersections only with theoretical quantities. The most appropriate experimental means to date to track electronic state mixing are time-resolved photoelectron spectroscopy [12] and high-harmonic spectroscopy [13]. The angle resolved photoelectron spectra, as well as the energy-resolved one, are well known to give very rich information about the electronic state transitions [14–16].

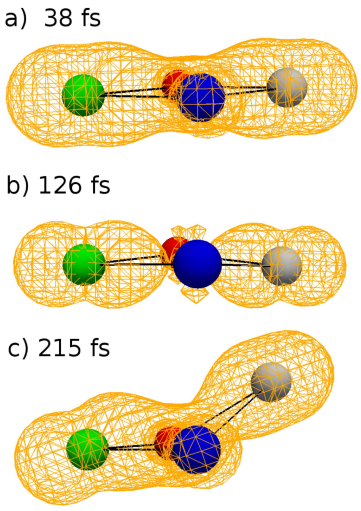

FIG. 4.6: Spatial distribution of unpaired electron density of S_b dynamics. Contour line is 0.03. Balls of gray, red, green, blue indicate, the nuclei of B1, B2, B3, B4 of Fig. 2.1, respectively.

We here study a possible induced emission spectrum to track the time evolution of electronic states. Although the SET cannot represent the path-branching dynamics, it has been shown that the electronic state mixing is very well reproduced by SET as long as the relevant path branching is not expected to be significant [17]. One can make use of this good property of SET to approximately deduce how the electronic state mixing can proceed qualitatively.

In the expansion of the total electron wavepacket in Eq. (3.1), here in this particular subsection, we choose the adiabatic wavefunctions $\Psi_I(\mathbf{r};\mathbf{R}(t))$ as expansion basis. Then the spectral lines are anticipated to be found at the energy $\Delta E_{0I} = E_I(\mathbf{R}(t)) - E_0(\mathbf{R}(t))$ (in the unit of cm^{-1}, it means ω_{0I}), where the suffix 0 denotes the ground state, with the intensity

$$\frac{2m\omega_{0I}}{3\hbar e^2}|\mu_{0I}|^2\,|C_I(t)|^2\,, \tag{4.1}$$

where μ_{0I} and ω_{0I} are the related dipole moment and frequency, respectively. We demonstrate in Fig. 4.7 such a spectral representation for the excited state. The weights $|C_I(t)|^2$ are summarized at each spectral line in this figure. It is well observed that starting from the single S_b state (top panel in Fig. 4.7), the total wavefunction is evolved in time to be a state of more and more complicated superposition of many adiabatic states. Although these spectra do not have quantitative accuracy, we clearly see the evolution of electronic state mixing caused by the nonadiabatic couplings. Well-designed stimulated emission experiments like the stimulated emission pumping spectroscopy (SEP) [18] should be able to detect the similar spectra, at least partly, and will give a powerful means to track the electron dynamics through nonadiabatic transitions.

Table 4.4: Eigenstate wavefunctions of S_b spectra.

	ΔE (cm^{-1})	Configuration	Coefficient		ΔE (cm^{-1})	Configuration	Coefficient
A	60719	$2a_g \rightarrow 2b_{2u}$	0.741	H	73873	$2a_g \rightarrow b_{3g}$	0.435
B	60608	$2a_g \rightarrow 2b_{2u}$	0.741			$1b_{1u} \rightarrow 2b_{2u}$	0.467
C	65729	$1b_{1u} \rightarrow 2b_{2u}$	0.848	I	47464	$2a_g \rightarrow 3a_g$	0.742
D	51774	$2a_g \rightarrow 3a_g$	0.660	J	55782	$1b_{1g} \rightarrow 3a_g$	0.716
E	55233	$2a_g \rightarrow 2b_{2u}$	0.491	K	59455	$2a_g \rightarrow 2b_{2u}$	0.532
		$1b_{1u} \rightarrow 2b_{2u}$	0.447			$1b_{1g} \rightarrow 2b_{2u}$	0.470
F	61762	$2a_g \rightarrow 2b_{2u}$	0.468	O	60951	$1b_{1g} \rightarrow 2b_{2u}$	0.592
		$1b_{1u} \rightarrow 3a_g$	0.587	P	64159	$1b_{1u} \rightarrow 3a_g$	0.680
G	72214	$2a_g \rightarrow b_{3g}$	0.615	Q	69384	$2a_g \rightarrow b_{3g}$	0.852

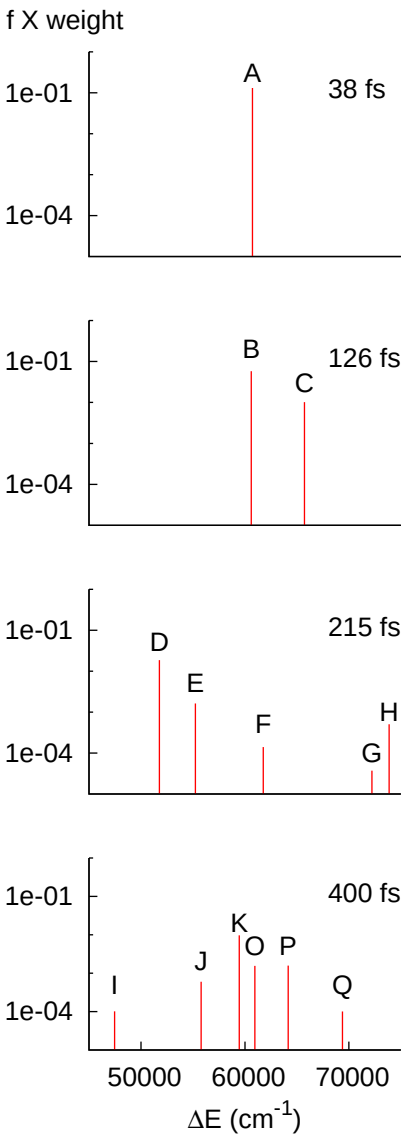

FIG. 4.7: Spectral representation of the time-evolution of S_b. The logarithmic values of the spectral intensity are plotted against the photo-emission energy. The state characters corresponding to the individual spectral line are summarized in Table 4.4.

4.3 Excited State: $^1B_{1u}$

The following two sections are nonadiabatic excited state dynamics studies in the states of S_d and S_g, which are similarly discussed to S_b case.

Giving zero point energy to $\omega_4(A_g)$ mode (0.08 ev), S_d started nonadiabatic dynamics is shown in Table 4.5 and Fig. 4.8. Similarly, the nuclear path associated with electronic behavior is analyzed as below. As $3a_g$∼$2b_{2u}$ starts to affect y-symmetry from 82 fs (4.1×10^{-4}, see Fig. 4.9), similar to that occurs in S_b case, just 5 fs is spent in passing through the quasi-D_{2h} state. Such an action can be seen as a characteristic behavior of $3a_g$∼$2b_{2u}$ interaction. Then, fresh symmetry-adapted configurations of $\Phi_n(B_2)$ and $\Phi_f(B_2)$ arises in the regular $C_{2v}(y)$ point group. But for the reason of double excitation, the population of $\Phi_l(B_2)$, $\Phi_n(B_2)$ and certainly $\Phi_m(B_2)$ is hard to increase markedly among the five displayed configurations. So the main interaction thereafter is $\Phi_d(B_2)$∼$\Phi_f(B_2)$ which really is $3a_g(a_1)$∼$2b_{2u}(a_1)$. As a result, vibration switches between $\omega_1(A_g)+\omega_5(B_{2u})$ and $\omega_4(A_g)+\omega_5(B_{2u})$.

Obviously, it is a relatively simply case that neither x-flux nor z-flux is induced during 400 fs and the dominant interactive realm spans merely the four frontier orbitals. However, if we notice the stable π radical, the interesting characteristic of S_d state can be understood. By comparasion with S_b case, it is easy for one to think that the difference is due to the initial kinetic energy. In S_b case, the $\omega_1(A_g)$ results in a smaller θ which implicates higher vibrational exciation energy. On the other hand, in S_d case the $\omega_4(A_g)$ extends the molecular framework that σ-π nonadiabatic interaction is weakened. It is a factor but not the root cause. Even if we replace initial mode with $\omega_1(A_g)$, S_d cannot induce obvious z-flux as S_b does. Though $1b_{1u}$ is initially excited in S_d, its partner $2a_g$ is hard to be excited sequentially. In D_{2h} section, the only symmetry-adapted single excitation correlating to $2a_g$ is $2a_g$→$2b_{1u}$, which is obviously unfavorable in energy. And then in $C_{2v}(y)$ group, even the most likely candidate of $2a_g(a_1)$→$b_{3g}(b_2)$ is still inexpectant. Since that implicates the vigorous $3a_g(a_1)$∼$2b_{2u}(a_1)$ would be replaced by $3a_g(a_1)$∼$b_{3g}(b_2)$ or $2b_{2u}(a_1)$∼$b_{3g}(b_2)$, what is unreasonable. From this point of view, it is the robust in-plane electronic behavior that unexpectedly ensures the stability of out-of-plane electron, what makes the stable π radical a necessity of S_d (see Fig. 4.10).

Table 4.5: Time sections of S_d started nonadiabatic dynamics.

S_d–I	0∼[82]∼87 fs (D_{2h})
Configurations (B_{1u})	Φ_d, Φ_l, Φ_m
Orbitals	$1b_{1u}$, $2a_g$, $3a_g$, $2b_{2u}$
Notes	$3a_g$∼$2b_{2u}$ begins to break y-symmetry after 82 fs.
S_d–II	87∼400 fs ($C_{2v}(y)$)
Configurations (B_2)	Φ_d, Φ_l, Φ_m, Φ_n, Φ_f
Orbitals	$1b_{1u}(b_2)$, $2a_g(a_1)$, $3a_g(a_1)$, $2b_{2u}(a_1)$
Notes	$3a_g(a_1)$∼$2b_{2u}(a_1)$ breaks y-symmetry at all after 87 fs.

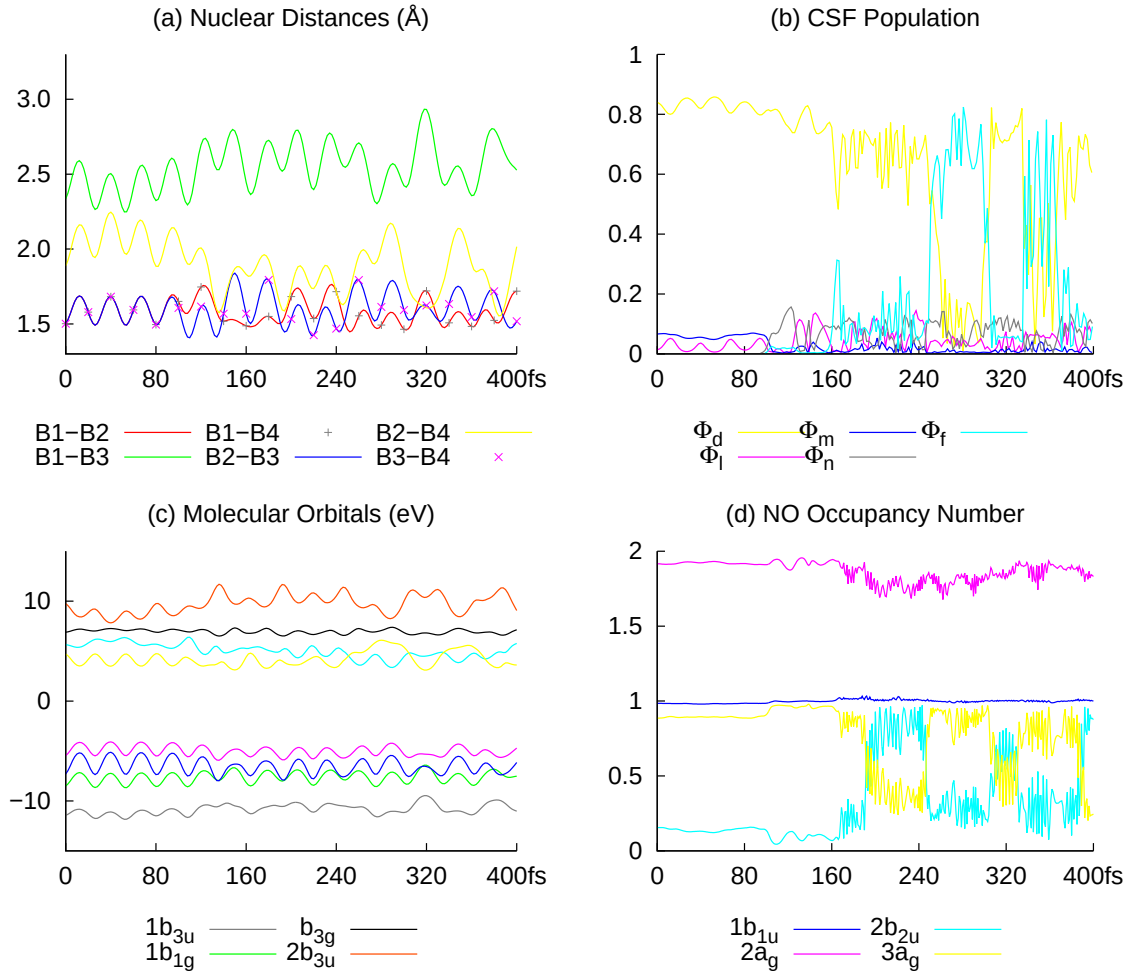

FIG. 4.8: Selected quantities of S_d started dynamics. panels (c) and (d) share the same key labels.

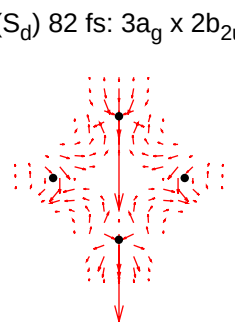

FIG. 4.9: Flux at selected time points of S_d dynamics: xy-section, z=0.0 bohr.

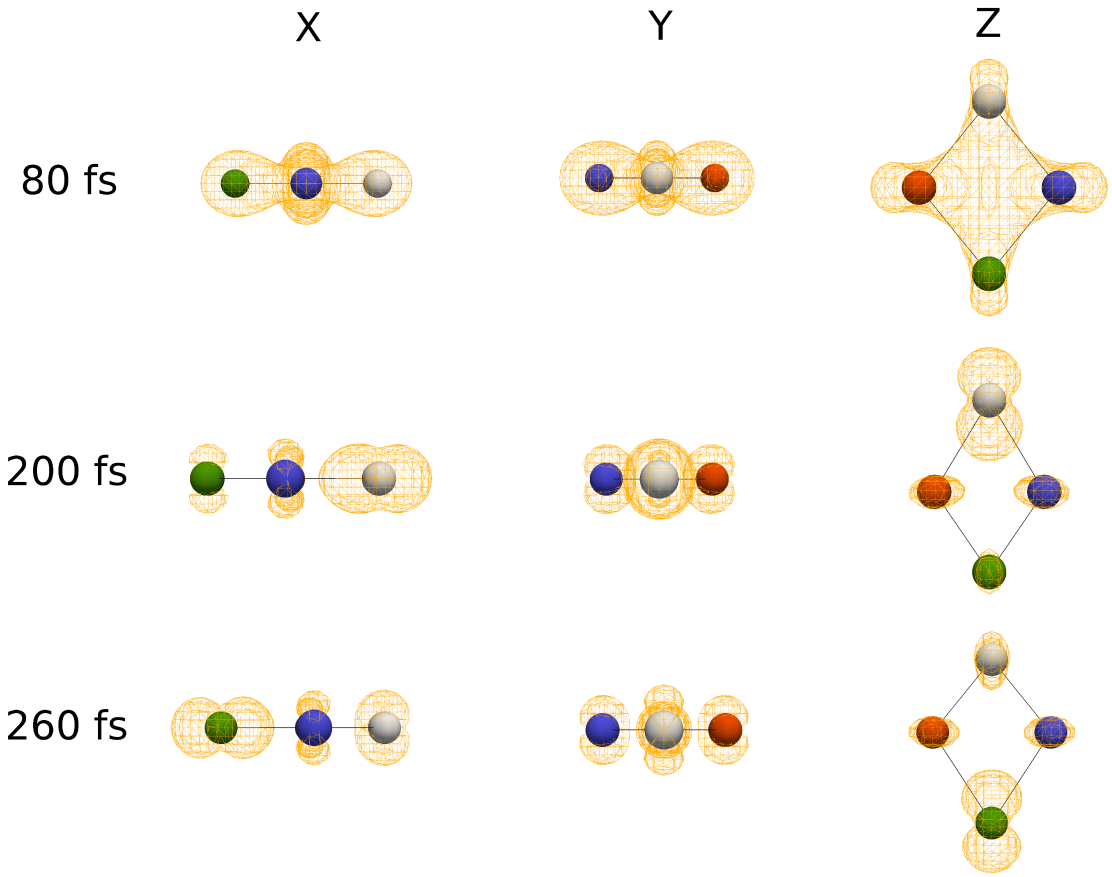

FIG. 4.10: Spatial distribution of unpaired electron density of S_d dynamics. Contour line is 0.03. Each panel shows a three-dimensional distribution viewed from +X, +Y, or +Z direction. Balls of gray, blue, green, red indicate, respectively, B1, B2, B3 and B4.

4.4 Excited State: $^1B_{3u}$

For S_g case, to observer an interesting behavior, the dynamics is selected starting from the stillness and the results are shown in Table 4.6 and Fig. 4.11. Same as S_b, occupied $2b_{2u}$ makes B_4 to be narrower and the molecule vibrates naturally along half-period $\omega_1(A_g)$ mode before symmetry-broken. But there is notable difference from S_b that the vibrational amplitude is larger in either edges or diagonals in spite of nothing initial kinetic energy is assigned. It can be explained by the NO bond order analysis of $1b_{1g}$ and $2a_g$ orbitals (see Fig. 4.3) that loss of electron from the former weakens all the bonds while the latter almost unaffectedly. Another important difference from previous is that the wavefunction actually proceeds with oscillations. It originates in the R_z-flux induced by $1b_{1g}$~$2a_g$ interaction. Empirically, if a flux induced up to 4×10^{-4} level towards an unitary direction lasts beyond 4 fs, the corresponding molecular symmetry could be affected. But in the current case, such a curl flux in the xy-plane prevents the x- or y-symmetry from being readily destroyed. As the y-flux begins to act at 86 fs (3.8×10^{-4} see Fig. 4.12), it is immediately cancelled out by R_z-flux (4.1×10^{-4}) and even be reversed soon by the oscillation. And the extended vibrational amplitude separates $3a_g$ from $2b_{2u}$ in energy making the interaction between them weaken, even the very capable $3a_g$~$2b_{2u}$ spends nearly 37 fs in breaking y-symmetry. Only after 123 fs, the molecule barely enters the $C_{2v}(y)$ group.

Once enter the $C_{2v}(y)$ group, $1b_{1g}(b_1)$~$2a_g(a_1)$ turns more domimnant at inducing x-flux. By virtue of the newcomer $\Phi_c(B_1)$, which causes $3a_g(a_1)$ more excited, strengthes $3a_g(a_1)$~$2b_{2u}(a_1)$ at 150 fs, and the y-symmetry escapes totally from troublesome interactions concerning about $1b_{1g}$ after 156 fs (see Fig. 4.12). At the same time, x-symmetry is broken to some extent which is enough to accept new configurations under the quasi-$C_s(xy)$ group and the really interesting part is yet to come.

The characteristic orbital of S_g state is $1b_{1g}$ which relates to $\omega_6(B_{1g})$ vibration. It requires at least a C_{2h} group and such a contidion is satisfied until enter $C_s(xy)$, which has a subgroup of C_{2h}. Recall Hückel MO energy evolution along $\omega_6(B_{1g})$ (Fig. 2.7). The two p_r-b_u orbitals corresponds to $2b_{2u}$ and $2b_{3u}$ respectively. If one of them becomes occupied, along $\omega_6(B_{1g})$ direction the pseudo-reflection *dsd* process (see panel (b) in Fig. 2.6) does not occur in rigious C_{2h} group. But in the current case, in-plane b_u symmetry has disappeared so that the $2b_{2u}(a^{'})$ and $2b_{3u}(a^{'})$ have the possibility to cross. Indeed they are. As half occupied $1b_{1g}(a^{'})$ caused $\omega_6(B_{1g})$ vibration proceeds, the crossing between $2b_{2u}(a^{'})$ and $2b_{3u}(a^{'})$ occurs evidently. Then $2b_{3u}(a^{'})$ becomes naturally occupied and the pseudo-reflection rearrangement inevitably happens. Such an excited state *dsd* process is accompanied by repeated bonding formation and dissociation (see Fig. 4.13).

Since z-flux has been discussed in S_b and the effect is not obvious here, interaction concerning p_π orbitals are negelected.

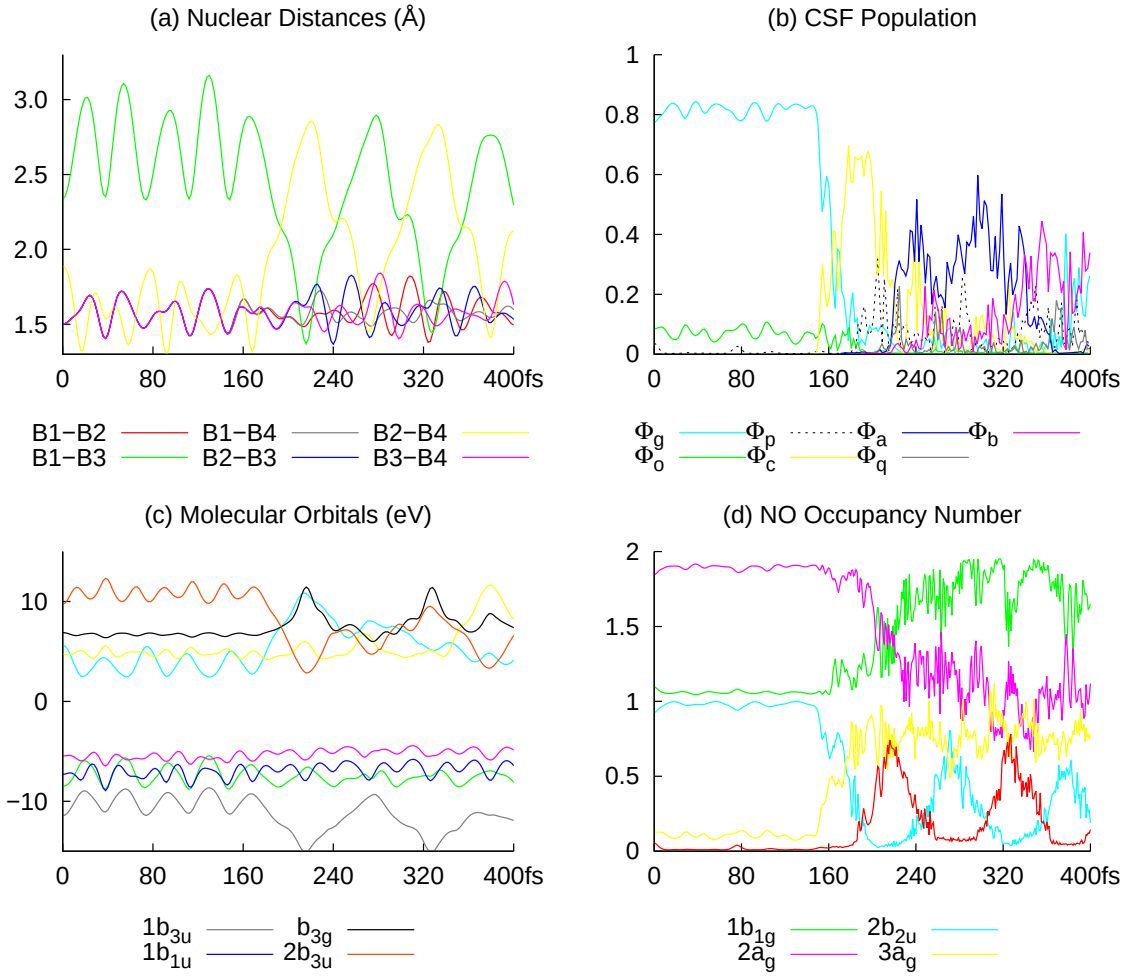

FIG. 4.11: Selected quantities of S_g started dynamics. (c) and (d) share the same key labels.

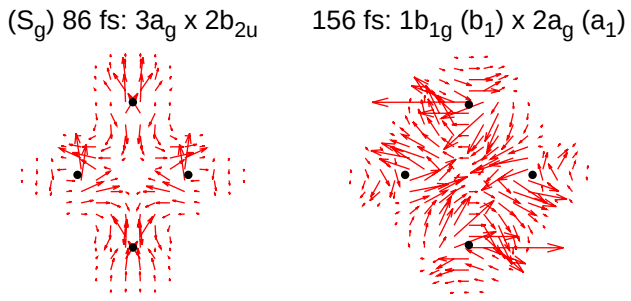

FIG. 4.12: Flux at selected time points of S_g dynamics: xy-section, z=0.0 bohr.

Table 4.6: Time sections of S_g started nonadiabatic dynamics.

S_g−I	0∼[86]∼123 fs (D_{2h})
Configurations (B_{3u})	Φ_g, Φ_o, Φ_p
Orbitals	$1b_{1g}$, $2a_g$, $3a_g$, $2b_{2u}$, $2b_{3u}$
Notes	$3a_g$∼$2b_{2u}$ begins to break y-symmetry after 86 fs.
S_g−II	123∼156 fs ($C_{2v}(y)$)
Configurations (B_1)	Φ_g, Φ_o, Φ_p, Φ_c
Orbitals	$1b_{1g}(b_1)$, $2a_g(a_1)$, $3a_g(a_1)$, $2b_{2u}(a_1)$, $2b_{3u}(b_1)$
Notes	$3a_g(a_1)$∼$2b_{2u}(a_1)$ breaks y-symmetry at all after 123 fs. $1b_{1g}(b_1)$∼$2a_g(a_1)$ begins to break x-symmetry after 123 fs.
S_g−III	156∼400 fs ($C_s(xy)$)
Configurations ($A^{'}$)	Φ_g, Φ_o, Φ_p, Φ_c, Φ_a, Φ_q, Φ_b
Orbitals	$1b_{1g}$ ($a^{'}$), $2a_g$ ($a^{'}$), $3a_g$ ($a^{'}$), $2b_{2u}$ ($a^{'}$), $2b_{3u}$ ($a^{'}$)
Notes	$1b_{1g}(a^{'})$∼$2a_g(a^{'})$ breaks x-symmetry to a certain extent after 156 fs.

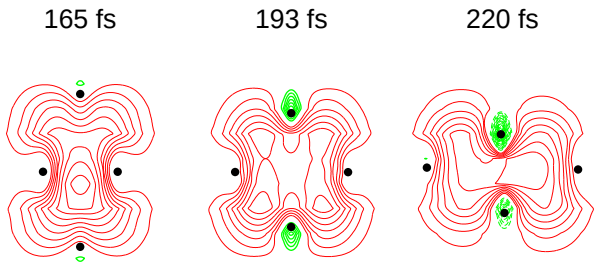

FIG. 4.13: Bond order density at selected time points of S_g dynamics: xy-section, z=0.0 bohr.

4.5 Conclusions

We have studied the dynamics of spatial symmetry breaking caused by a series of passages through symmetry-allowed conical intersections in the low-lying excited states of cyclic-B_4 molecule.

Prior to a real-time track of the nonadiabatic transitions, we attempted to characterize the molecular symmetry in terms of the Hückel molecular orbitals because of their very transparent and simple properties in a way for them to be built from atomic orbital basis functions to molecular orbitals. Among six occupied valence orbitals, one σ and one π 4c-2e orbitals and four sp hybridization orbitals are reproduced by Hückel theory. It suggests that such a way of bonding is necessary to form electron-deficient bonds of B_4, which makes a stable four-member ring without relying on the deltahedral structure of boron. Besides, the study suggests that the Hückel method can be used

to foresee what kind of conical intersections may exist. This is because wavefunctions consisting of the Hückel molecular orbitals can be regarded as the simplest approximation to the diabatic bases. Although either the crossing energy or location is not numerically accurate, if used appropriately, it is quite instructive.

Then we attempted to track the symmetry-breaking nonadiabatic dynamics from the view point of electron dynamics. Actually we applied the semiclassical Ehrenfest theory, which cannot follow path-branching dynamics. We have first examined the feature of the potential curves in the reaction retaining D_{2h} symmetry, and observed a rich yet clear structure of conical intersections among seven low-lying states. By dissecting the marked areas where transition occurs, it is found that the nonadiabatic process usually obeys the following procedures: (1) As molecule vibrates, nuclear kinematic interactions generate asymmetric electronic flux. (2) Accumulated asymmetric flux starts to affect the molecular symmetry at a quasi-symmetric state. (3) Once the symmetry is slightly destroyed, the forbidden interactions turn to be allowed and enhance the flux more. (4) Thus enhanced flux breaks the symmetry to larger extent.

It has been suggested that such time evolution of the electron wavepackets through nonadiabatic state-mixing may be able to be detected by time-dependent induced photoemission in electronic spectroscopy. We have demonstrated the time-series of an "assumed instantaneous emission spectrum" by calculating the spectral positions and the associated intensities as well of B_4 molecule.

We hope the present work serves as a very basic building block with which to construct more large-scale quantitative study for nonadiabatic dynamics through symmetry-allowed conical intersections in excited state chemical reactions.

Reference

[1] P. Löwdin, Phys. Rev. 97 (1955) 1474.

[2] P. Löwdin, Phys. Rev. 97 (1955) 1490.

[3] M. W. Schmidt, K. K. Baldridge, J. A. Boatz, S. T. Elbert, M. S. Gordon, J. H. Jensen, S. Koseki, N. Matsunaga, K. A. Nguyen, S. J. Su, T. L. Windus, M. Dupuis, and J. A. MOntgomery, J. COMPUT. CHEM. 14 (1993) 1347.

[4] A. N. Alexandrova, A. I. Boldyrev, H. Zhai and L. Wang, Coord. Chem. Rev. 250 (2006) 2811.

[5] M. M. Balakrishnarajan, and R. Hoffmann, J. Am. Chem. Soc. 126 (2004) 13119.

[6] H. Reis, and M. G. Papadopoulos, J. Comput. Chem. 20 (1999) 679.

[7] H. Jin, and Q. Li, Phys. Chem. Chem. Phys. 5 (2003) 1110.

[8] H. Zhai, L. Wang, A. N. Alexandrova, A. I. Boldyrev, and V. G. Zakrzewski, J. Phys. Chem. A 107 (2003) 9319.

[9] P.W. Fowler, R. W. A. Havenith, and E. Steiner, Chem. Phys. Lett. 359 (2002) 530.

[10] H. Braunschweig, V. Dyakonov, J. O. C. Jimenez-Halla, K. Kraft, I. Krummenacher, K. Radacki, A. Sperlich, and J. Wahler, Angew. Chem. Int. Ed. 51 (2012) 2977.

[11] D. Lu, C. Wu, and P. Li, Chem. Eur. J. 20 (2014) 1630.

[12] T. Horio, T. Fuji, Y.-I. Suzuki, and T. Suzuki, J. Am. Chem. Soc. 131 (2009) 10392.

[13] P. M. Kraus, Y. Arasaki, J. B. Bertrand, S. Patchkovskii, P. B. Corkum, D. M. Villeneuve, K. Takatsuka, and H. J. Wöner, Phys. Rev. A 85 (2012) 043409.

[14] K. Takatsuka, T. Yonehara, K. Hanasaki, and Y. Arasaki, Chemical Theory beyond the Born-Oppenheimer Paradigm (World Scientific, Singpore, 2015).

[15] Y. Arasaki, K. Takatsuka, K. Wang, and V. McKoy, Phys. Rev. Lett. 90 (2003) 248303.

[16] Y. Arasaki, K. Takatsuka, K. Wang, and V. McKoy, J. Chem. Phys. 119 (2003) 7913.

[17] T. Yonehara, and K. Takatsuka, J. Chem. Phys. 128 (2008) 154104.

[18] C. E. Hamilton, J. L. Kinsey, and R. W. Field, Annu. Rev. Phys. Chem. 37 (1986) 493.

Chapter 5

General Conclusions

This thesis employs *ab initio* nonadiabatic electron dynamics method developed from semiclassical Ehrenfest theory to study the symmetry-breaking process of cyclic-B_4 cluster. We simultaneously track the nuclear path and the electronic wavepackets (in terms of such as configuration population, occupancy number of natural orbitals, and probability current, etc.). By analyzing the interactions among them, numerical results show that the kinetic-coupling terms are the key to break the symmetric electronic Hamiltonian, which agrees with the fundamental rule of quantum mechanism. Briefly speaking, symmetric nuclear vibration generates asymmetric electron flow through the kinetic-coupling term and *vice versa* the induced asymmetric electron flow affects the symmetric nuclear configuration. So the kinetic-coupling can be also called "friction"term. Symmetry rules in the Group theory direct the reaction throughout the process.

One may doubt that how accurate the numerical results are. Indeed it is necessary to point out the limitations when employ a theoretical method. Prior to the dynamics chapter, Hückel theory is used to identify the irreducible representations and gives a useful and instructive result. As seen from Fig. 2.9(b) and Fig. 4.2, the Hückel predicted conical interactions can be accepted just at the level of the symmetric characteristics of electronic states. For crossing energy, it is undependable. However, for large scale molecules (especially those have any symmetries), a Hückel guess on the locations of the conical interactions along any particular reaction coordinates may be a good reference qualitatively for more expensive calculations. For example, tell people in which direction there should be conical interactions. Besides, all the time points mentioned in the dynamics are very sensitive to numerical calculations such as integration schemes, initial conditions or even the machines. Since the processes those pass through the avoided crossing areas are highly nonlinear. Thus, rather than focus on how many femtoseconds a process exactly take (38 fs, or 36 or 40 fs), the key issue is the certain phenomena appeared in the characteristic electronic state. For example, the z-symmetry must be broken prior to the y- and the x-symmetry-breaking in the $^1B_{2u}$ state case. So,

we actually created nothing new rule. The numerical study is just a tool to discovery the existing but unrevealed connections among the concepts such as kinetic-coupling, conical interactions and the Group theory and visualize them.

At last, here we take a brief introduction of next work. The present thesis studies the symmetry-breaking process using cyclic-B_4 as a case since it is a high symmetric molecule. *Vice verse*, how the symmetry-generating process works? This time take B_6 for instance, which has no stationary planar structure at the singlet ground state state. This is due to the essential of hexa-atom molecule which can be illustrated by the Hückel theory too. One of the ground state stationary structure of B_6 is C_2 symmetry, which is non-planar. Interestingly, once excited, the molecule may transform into various quasi-planar geometries such as C_{2v}, C_{2h} or even D_{2h} alike. Tracking these processes may be a complement to the present thesis, what is underway.

Appendix A

These derivations are referred by section 3.2.

A1. Derivation of $X_{IJ}^k = \sum_{ij}^{\mathrm{MO}} a_{ij}^{IJ}(U_{ij}^k + S_{ij}^{kR})$

First use one-electron constant to reduce the derivative coupling integral from CSF bases to MO bases as

$$X_{IJ}^k = \langle \Phi_I | \partial_k | \Phi_J \rangle = \sum_{ij}^{\mathrm{MO}} a_{ij}^{IJ} \langle \phi_i | \partial_k | \phi_j \rangle = \sum_{ij}^{\mathrm{MO}} a_{ij}^{IJ} d_{ij}^k, \tag{5.1}$$

wherein

$$d_{ij}^k = \langle \phi_i | \partial_k | \phi_j \rangle = \big\langle \sum_{\mu}^{\mathrm{AO}} c_\mu^i \chi_\mu \big| \partial_k \big| \sum_{\nu}^{\mathrm{AO}} c_\nu^j \chi_\nu \big\rangle = \sum_{\mu\nu}^{\mathrm{AO}} c_\mu^i c_\nu^j \langle \chi_\mu | \partial_k \chi_\nu \rangle + \sum_{\mu\nu}^{\mathrm{AO}} c_\mu^i (\partial_k c_\nu^j) \langle \chi_\mu | \chi_\nu \rangle. \tag{5.2}$$

By the definition of Eq. (3.19), we have

$$\begin{aligned}
S_{ij}^k &= \sum_{\mu\nu}^{\mathrm{AO}} c_\mu^i c_\nu^j \langle \chi_\mu | \partial_k \chi_\nu \rangle + \sum_{\mu\nu}^{\mathrm{AO}} c_\mu^i c_\nu^j \langle \partial_k \chi_\mu | \chi_\nu \rangle \\
&= d_{ij}^k - \sum_{\mu\nu}^{\mathrm{AO}} c_\mu^i (\partial_k c_\nu^j) \langle \chi_\mu | \chi_\nu \rangle + \sum_{\mu\nu}^{\mathrm{AO}} c_\mu^i c_\nu^j \langle \partial_k \chi_\mu | \chi_\nu \rangle \\
&= d_{ij}^k - \sum_{\mu\nu}^{\mathrm{AO}} c_\mu^i (\sum_{m}^{MO} c_\nu^m U_{mj}^k) \langle \chi_\mu | \chi_\nu \rangle + \sum_{\mu\nu}^{\mathrm{AO}} c_\mu^i c_\nu^j \langle \partial_k \chi_\mu | \chi_\nu \rangle \\
&= d_{ij}^k - \sum_{m}^{MO} U_{mj}^k (\sum_{\mu\nu}^{\mathrm{AO}} c_\mu^i c_\nu^m) \langle \chi_\mu | \chi_\nu \rangle + \sum_{\mu\nu}^{\mathrm{AO}} c_\mu^i c_\nu^j \langle \partial_k \chi_\mu | \chi_\nu \rangle \\
&= d_{ij}^k - \sum_{m}^{MO} U_{mj}^k (S_{im}) + \sum_{\mu\nu}^{\mathrm{AO}} c_\mu^i c_\nu^j \langle \partial_k \chi_\mu | \chi_\nu \rangle \\
&= d_{ij}^k - \sum_{m}^{MO} U_{mj}^k (\delta_{im}) + \sum_{\mu\nu}^{\mathrm{AO}} c_\mu^i c_\nu^j \langle \partial_k \chi_\mu | \chi_\nu \rangle \\
&= d_{ij}^k - U_{ij}^k + \sum_{\mu\nu}^{\mathrm{AO}} c_\mu^i c_\nu^j \langle \partial_k \chi_\mu | \chi_\nu \rangle.
\end{aligned} \tag{5.3}$$

Considering another important relation between S_{ij}^k and U_{ij}^k by Eq. (3.33), d_{ij}^k is expressed as

$$d_{ij}^k = -\sum_{\mu\nu}^{\mathrm{AO}} c_\mu^i c_\nu^j \langle \partial_k \chi_\mu | \chi_\nu \rangle - U_{ji}^k. \tag{5.4}$$

On the other hand, since $\langle\phi_i|\phi_j\rangle = \delta_{ij}$ (the orthogonality of MO), its nuclear derivative is zero; namely $\partial_k\langle\phi_i|\phi_j\rangle = 0$. This gives the relation of

$$\langle\partial_k\phi_i|\phi_j\rangle = -\langle\phi_i|\partial_k\phi_j\rangle = \langle\phi_j|\partial_k\phi_i\rangle^\star = \langle\phi_j|\partial_k\phi_i\rangle, \tag{5.5}$$

and the last step is due to their real numbers in numerical calculation. Thus the definition of d_{ij}^k in Eq. (5.2) becomes

$$d_{ij}^k = \frac{1}{2}(\langle\phi_i|\partial_k|\phi_j\rangle - \langle\phi_j|\partial_k|\phi_i\rangle). \tag{5.6}$$

Note that it is antisymmetric matrix which has the relation of

$$d_{ij}^k = -d_{ji}^k. \tag{5.7}$$

So Eq. (5.4) can be rewritten as

$$d_{ij}^k = \sum_{\mu\nu}^{\mathrm{AO}} c_\mu^i c_\nu^j \langle\chi_\mu|\partial_k\chi_\nu\rangle + U_{ij}^k = S_{ij}^{kR} + U_{ij}^k, \tag{5.8}$$

herein use the relation of real matrix that $\langle\partial_k\chi_\mu|\chi_\nu\rangle = \langle\chi_\nu|\partial_k\chi_\mu\rangle^\star = \langle\chi_\nu|\partial_k\chi_\mu\rangle$ and then interchang subscripts. So far Eq. (3.13) has been deduced.

A2. Derivation of $S_{ij}^{kR} = S_{ji}^{kL}$

$$S_{ij}^{kR} = \sum_{\mu\nu}^{\mathrm{AO}} c_\mu^i c_\nu^j \langle\chi_\mu|\partial_k\chi_\nu\rangle = \sum_{\mu\nu}^{\mathrm{AO}} c_\mu^i c_\nu^j \langle\partial_k\chi_\nu|\chi_\mu\rangle = \sum_{\mu\nu}^{\mathrm{AO}} c_\nu^i c_\mu^j \langle\partial_k\chi_\mu|\chi_\nu\rangle = S_{ji}^{kL} \tag{5.9}$$

wherein use the relation of real matrix: $\langle\chi_\mu|\partial_k\chi_\nu\rangle = \langle\partial_k\chi_\nu|\chi_\mu\rangle^\star = \langle\partial_k\chi_\nu|\chi_\mu\rangle$ and then interchang subscripts.

A3. Derivation of $U_{ij}^a + U_{ji}^a + S_{ij}^a = 0$

Since $S_{ij} = \delta_{ij}$, so $\partial_a S_{ij} = 0$. On the other hand,

$$\begin{aligned}
\frac{\partial S_{ij}}{\partial a} &= \frac{\partial}{\partial a}\sum_{\mu\nu}^{\mathrm{AO}} c_\mu^i c_\nu^j S_{\mu\nu} \\
&= \sum_{\mu\nu}^{\mathrm{AO}} c_\mu^i c_\nu^j \partial_a S_{\mu\nu} + \sum_{\mu\nu}^{\mathrm{AO}} (\partial_a c_\mu^i) c_\nu^j S_{\mu\nu} + \sum_{\mu\nu}^{\mathrm{AO}} c_\mu^i (\partial_a c_\nu^j) S_{\mu\nu} \\
&= \sum_{\mu\nu}^{\mathrm{AO}} c_\mu^i c_\nu^j \partial_a S_{\mu\nu} + \sum_{\mu\nu}^{\mathrm{AO}} \big(\sum_m^{\mathrm{MO}} c_\mu^m U_{mi}^a\big) c_\nu^j S_{\mu\nu} + \sum_{\mu\nu}^{\mathrm{AO}} c_\mu^i \big(\sum_m^{\mathrm{MO}} c_\nu^m U_{mj}^a\big) S_{\mu\nu} \\
&= \sum_{\mu\nu}^{\mathrm{AO}} c_\mu^i c_\nu^j \partial_a S_{\mu\nu} + \sum_m^{\mathrm{MO}} \big(U_{mi}^a \sum_{\mu\nu}^{\mathrm{AO}} c_\mu^m c_\nu^j S_{\mu\nu} + U_{mj}^a \sum_{\mu\nu}^{\mathrm{AO}} c_\mu^i c_\nu^m S_{\mu\nu}\big) \\
&= S_{ij}^a + \sum_m^{\mathrm{MO}} (U_{mi}^a S_{mj} + U_{mj}^a S_{im}) \\
&= S_{ij}^a + \sum_m^{\mathrm{MO}} (U_{mi}^a \delta_{mj} + U_{mj}^a \delta_{im}) \\
&= S_{ij}^a + U_{ji}^a + U_{ij}^a.
\end{aligned} \tag{5.10}$$

Appendix B

Abstract

The first singlet excited state geometries of various isomers and tautomers of firefly oxyluciferin ($OxyLH_2$), as well as their fluorescence spectra in aqueous solution, were studied using time dependent density functional theory (TDDFT). With changing pH in aqueous solution, three fluorescence peaks, blue (450 nm), yellow-green (560 nm), and red (620 nm) correspond to neutral keto and enolic forms, the monoanionic enolic form, and the monocationic keto form respectively. A counterion, Na^+, was predicted to cause a blue shift in the fluorescence of anionic $OxyLH_2$. The contributions of a charge transfer (CT) state upon electronic excitation of the planar and twisted structures were predicted. CT was large for the twisted structures but small for the planar ones. The differences between pK and pK^* of various oxyluciferin species were predicted using a Forster cycle. A new possible light emitter, namely, the monocation keto form (keto+1), was considered.

B1. Introduction

Bioluminescence and Chemiluminescence

The bioluminescence produced by various natural firefly luciferases and their mutants range in color from green (∼530nm) to red (∼635nm) [1–6]. The most accepted mechanism is that the reaction of firefly luciferin (LH_2), which binds to the active site of firefly luciferases and in the presence of ATP, Mg^{2+}, and O_2, is catalyzed by the enzyme resulting in an electronic excited state oxyluciferin ($OxyLH_2$) (see Fig. 5.1). The reaction proceeds via a highly energetic dioxetanone intermediate formed by chemically initiated electron-exchange luminescence (CIEEL) [7–10]. Visible light is emitted as the first excited singlet state (S_1) of $OxyLH_2$ decays to the ground state (S_0). A topic of great interest is the exact nature of the interactions between luciferases and luciferin which cause the same substrate to emit multicolor light.

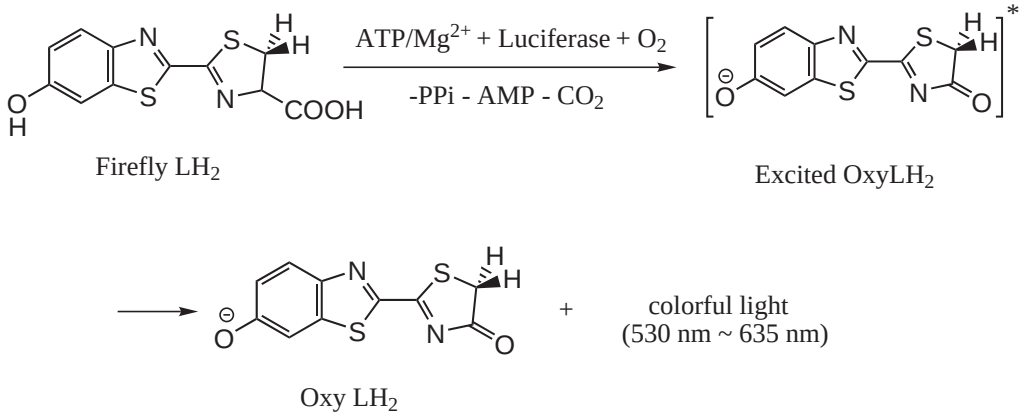

FIG. 5.1: Supposed mechansim in bioluminescence of firefly.

In early studies due to the complexity of the biosystem, attempts to reveal the details of the enzymatic reactions using radioactive substrates and spectroscopic techniques failed [9, 11]. Later the chemiluminescence of firefly luciferin-AMP (or its analogs), in basic solvent (potassium tert-butoxide in dimethylsulfoxide (DMSO) or imidazolate in water) and oxygen, was examined in detail in the laboratory (see Fig. 5.2) [4, 9, 11]. Taking the chemiluminescence in DMSO as an example, the peak of emission spectrum changes shifts red (630nm) to yellow-green (555nm) with an increase in the amount of potassium *tert*-butoxide [4, 9, 11–15]. One explanation invoked two tautomers, *viz.* the keto and enol forms with the equilibrium determined by the concentration of the base: keto emits red and enol yellow-green light. Given the similarity of the emission spectra between chemi- and bio- luminescence, their mechanisms were thought to be the same, namely pH-dependent keto-enol tautomerism [11–13].

So, $OxyLH_2$ was synthesized long ago and its absorption and fluorescence spectra were measured in various solvents (such as ethanol, DMSO, and water at different pH) to obtain more detailed information on the color modulation [16–18]. IR and NMR showed that $OxyLH_2$ exists as an enolic form in neutral media (see Fig. 5.3) [19]. The 371 nm and 425 nm absorption peaks in DMSO correspond to the neutral enolic form and to this species after deprotonation at 6′-H [20]. In aqueous solution, these two absorption peaks shift to 370 nm and 415 nm [17]. The 10 nm blue shift of the anionic enolic form is caused by increasing solvent polarity and is supported by theoretical results [21, 22]. On the other hand, fluorescence peaks at 450 nm and 570 nm in aqueous solution correspond to enol0 and its form with deprotonation at 6′-H. The 620 nm peak was thought to be produced by the keto form [17]. Later the 570 nm peak was separated into 556 nm and 587 nm peaks, which correspond to enol-2 and enol-1 [23].

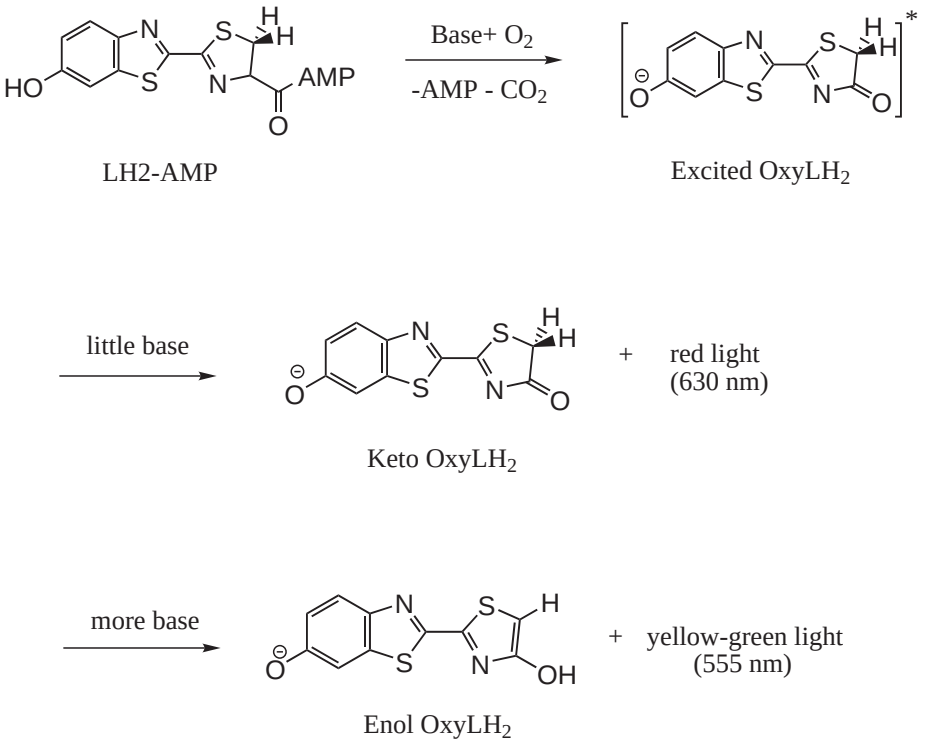

FIG. 5.2: Supposed mechanism in chemiluminescence of luciferin-AMP.

Emission Spectra in Solvent

Interestingly, previous theoretical studies did not agree with these results very well. For example, according to SAC-CI (symmetry-adapted cluster-configuration interaction) and CASSCF (complete active space self-consistent field) and TDDFT (time-Dependent density functional theory), enol-1 always has a lower emission energy than keto-1 and enol-2 has the lowest emission energy [21,24,25]. At the same time, it was reported that 5,5-dimethyl-$OxyLH_2$, an analogue of $OxyLH_2$ which could emit only red light (630 nm) in chemiluminescence according to the tautomerism model as it exists only in the keto form, was found to emit yellow-green light (560 nm) with luciferase [1]. A theoretical explanation of this result involved the nearby protein residues and AMP with the electrostatic effect of the protein causing the keto form to be a higher energy emitter [24]. Furthermore, Nakatsu et al. reported on the basis of X-ray structural analyses of firefly luciferases that green (560 nm) and red light (613 nm) correspond to tight and loose structures of the active sites respectively [2]. Thus the tautomerism mechanism seems not be necessary to explain the multicolor bioluminescence of firefly luciferins. On the other hand, Ando et al. found that red emission components (620 nm peak and 670 nm peak) were insensitive to pH implicating that pH-sensitive luciferases remain important in studies of bioluminescence [26]. In a word, the details of tautomerism and the fluorescence spectra of oxyluciferin in solvent need to be expounded further prior to considering the even more complicated

case of bioluminescence.

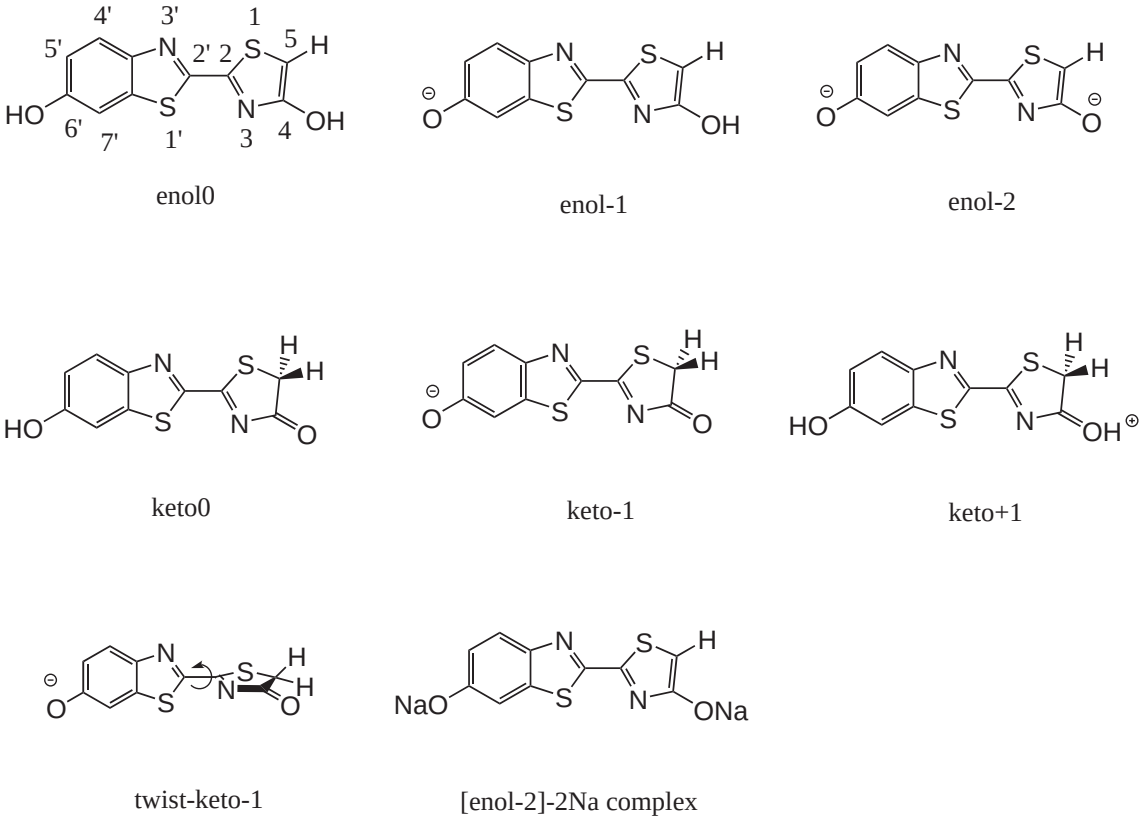

FIG. 5.3: Forms of oxyluciferin and its analogues.

Proton transfer (PT) and excited state intramolecular proton transfer (ESIPT) are the keys to understanding tautomerism. PT can be analyzed in terms of the pK and pK^* values of corresponding $OxyLH_2$ species. A Forster cycle [27] is employed here to study the changes in acidity and basicity of $OxyLH_2$ from the ground state to the lowest excited state. Further, the predicted emission spectra are compared with experimental emission spectra to explain the multicolor fluorescence of $OxyLH_2$.

In addition, luciferin-AMP in water with imidazole and in DMSO with potassium tert-butoxide produce similar red chemiluminescence (λ_{max}= 650 nm and λ_{max}= 630 nm respectively) [9]. The emitter was thought to be keto-1 and the blue shift in λ_{max} appeared to be in a progression from more to less polar surroundings [11,12]. However, the predicted shift was to the red with decreasing solvent polarity [21,24]. Therefore, other factors that can lead to different shifts in the wavelengths are assessed such as changes in pH, or the effects of a counter ion [17], Na^+.

Density functional theory (DFT) and TDDFT are employed to predict the ground and excited states of $OxyLH_2$. Previously some properties of $OxyLH_2$ were predicted with similar methods [22]. This work adopts another point of view. Notably, TDDFT has been criticized for its predictions

on $OxyLH_2$ due to the possibility of charge transfer (CT) states for which TDDFT with the usual exchange-correlation functionals is known to have difficulties [25,28,29]. Herein, any CT contribution to the excited state is examined before employing TDDFT.

B2. Computational Methods

Spectrum Prediction

The 6-31+G* basis set, which includes diffuse functions and *d*-type polarization functions, was employed except for molecules containing Na where the 6-31G* set was used instead.

All the S_0 geometries of $OxyLH_2$ species were optimized [30] by B3LYP [34] (Becke's hybrid exchange functional and the correlation functional of Lee, Yang, and Parr) in Gaussian03 [35]. The S_1 geometries were optimized with TD B3LYP in Turbomole [36]. The local correlation function SVWN3 or SVWN5 in B3 depends on whether Gaussian03 or Turbomole was used. SVWN3 is included in B3 Gaussian03 and SVWN5 in B3 in Turbomole. For $OxyLH_2$ molecules, the results with the two functionals were compared and there is no significant difference on geometric predictions.

In order to consider solvent effects on excitation energies, the polarized continuum model (PCM) [37, 38] in Gaussian03 was adopted but not the conductor-like screening model (COSMO) which interfaces with Turbomole. So excitation energy predictions were performed with TD B3LYP in Gaussian03.

Charge Transfer State

Before using TDDFT to predict $OxyLH_2$ emission energies, a possible problem needs to be addressed. LH_2 was found to have a CT state as its first excited state [39]. Thus TDDFT may underestimate excitation energies of $OxyLH_2$ due to possible CT contributions [24, 25] similar to the case of LH_2. Herein, charge distribution analysis was carried out. As a specific example, at the TD B3LYP optimized S_1 geometries of keto-1 (TDDFT may still be effective in geometry optimization although its energy prediction of the CT state is somewhat contentious [40]), atomic charge distributions were predicted for the essentially planar structures (which are minima in both S_1 and S_0 [21, 22, 24, 25]) and twisted structure (which once was assigned to the red emitter but recently discounted due to the small oscillator strengths of the $S_1 \rightarrow S_0$ transition [24, 25], see Fig. 5.3) by CIS (configuration interaction with single excitations) method. The planar form showed a small CT contribution, with only 0.118 negative charges transferred from the benzothiazole moiety to the thiazoline. In contrast 0.708 electrons were transferred in twisted keto-1, which was thought to possess a twisted charge transfer (TICT) state upon electronic excitation. The CT contribution in the planar $OxyLH_2$ species is small and TDDFT should be adequate for predicting the electronic excitations. Further indication of the adequacy of TD B3LYP for the prediction of the emission of keto-1 at 556 nm comes from

comparison with the previous CASSCF result [25] of 527 nm.

When discussing the effects of counter ions on the excited state geometries of $OxyLH_2$ Na-complexes the PCM water model must be included. However, large CT occurs from $OxyLH_2$ to Na upon excitation in the gas phase. Thus, in order to employ PCM during excited state geometry optimization, CIS in Gaussian03 was adopted.

B3. Fluorescence of Oxyluciferin in Aqueous Solution

Identify Fluorescence Emitters

Now consider the absorption spectra and the steady state fluorescence spectra of $OxyLH_2$ in actual aqueous solutions. The spectra are mainly affected by changes in pH (Table 5.1).

Table 5.1: Predicted absorption and emission spectra, λ_{max}, in nm, and oscillator strengths, f, predicted for $OxyLH_2$ in PCM water with TD B3LYP/6-31+G*.

	absorption spectra[a]					emission spectra		
	water/gas[b]		water/water		exp [17]	water/gas		exp [17]
	λ_{max}	f	λ_{max}	f	λ_{max}	λ_{max}	f	λ_{max}
enol0	388	0.66	389	0.66	370	454	0.66	450
keto0	411	0.43	420	0.45		459	0.30	
enol-1	489	0.75	478	0.69	415	508	0.60	560
keto-1	507	0.80	512	0.77		559	0.57	
enol-2	499	0.57	495	0.58		573	0.48	
keto+1	517	0.33	517	0.31		606	0.08	620

[a] Absorption spectra predicted by TD B3LYP/6-31+G*//B3LYP/6-31+G*; and emission spectra by TD B3LYP/6-31+G*// TD B3LYP/6-31+G*. [b] Water/gas means an excitation energy calculation in PCM water based on geometry optimization in the gas phase. Similarly, water/water means an excitation energy calculation in PCM water based on geometry optimization in PCM water.

The two absorption wavelength maxima, 370 nm in acidic and 415 nm in basic solutions, indicate there were at least two ground state species, that probably correspond to the neutral form and that deprotonated at 6′-H, namely enol0 and enol-1. The 4-H in enol-1 is unlikely to be deprotonated for there is no change in the maximum wavelength upon increasing the pH, while the absorption spectrum of enol-2 was predicted to red shift (approximately 15 nm) compared with the monoanions. Comparing the results of water/gas and water/water for $OxyLH_2$ molecules, the PCM solvent model causes only small changes in the absorption spectra after geometry optimization. Thus, for excited

state geometry optimization, solvent effects on geometries were not included and computations were of the type water/gas.

In experiments the fluorescence spectra exhibited three wavelength maxima at different pH (pH>9, 560 nm; 8>pH>3, 450 nm; pH<3, 620 nm). The maximum at 450 nm (blue fluorescence) should be produced by enol0 as supported by the TDDFT predictions and the experiments, considering that only blue fluorescence was observed in ethanol [17], which inhibited proton transfer, or with $MeOLH_2$ (6′-methoxyluciferin), which has no 6′-H for deprotonation. With increasing pH, enol0 is doubtlessly ionized to enol-1 and the maximum at 560 nm (yellow-green fluorescence) likely corresponds to enol-1. Note keto-1 has more reasonable predicted emission spectrum comparing with experiment. If it is the yellow-green light emitter, excited state PT or hydrogen migration mechanism between enol-1 and keto-1 needs further studied. Here only discuss the changes of the acidity and the basicity of them upon excitation. For example, could such a ionization occur in the excited state? Will the monoanion (enol-1) transform into a dianion (enol-2) before a radiative transition? The pK_a^* (superscript of aster denotes excited state) for the 6′-H was thought to decrease upon electronic excitation [4, 9, 15, 17, 23, 41]. A Forster cycle [27], which incorporates the acidity and the basicity of various species of $OxyLH_2$, is given in Fig. 5.4 and used to discuss changes from pK to pK^*.

Taking enol0 and enol-1 as examples, together with enol0* and enol-1*, corresponding Forster cycle is illustrated on the left-hand side of Fig. 5.4. ΔE_{deprot} and $\Delta E^*_{\text{deprot}}$ are the energies required for deprotonation of enol0 in S_0 and S_1 states respectively. The smaller the deprotonation energy, the higher the acidity of either electronic state. So the value of $\Delta\Delta E_{\text{deprot}}$, which is the difference between ΔE_{deprot} and $\Delta E^*_{\text{deprot}}$, implicates the acidity change of enol0 upon electronic excitation. Similarly, taking the cycle of keto0 and keto+1 on the right-hand side of Fig. 5.4 as an example, ΔE_{prot} and ΔE^*_{prot} are the energies released upon protonation of keto0. The more energy that is released, the higher the basicity of keto0. So the value of $\Delta\Delta E_{\text{prot}}$, which is the difference between ΔE_{prot} and ΔE^*_{prot}, implicates the basicity change of keto0 upon electronic excitation.

Fig. 5.4 shows the energy values associated with the following different cycles and provides the information as below:

1. The acidity of 6′-H in enol0 increases markedly upon electronic excitation as well as in keto0: $\Delta\Delta E_{\text{deprot(enol0)}} = 0.59$ ev, $\Delta\Delta E_{\text{deprot(keto0)}} = 0.54$ ev. So the ionization of 6′-H could occur in the excited state.

2. If enol-1 or keto-1 do not lose the proton in the ground state, it is impossible for them to transform to enol-2 by deprotonation in the excited state as they show less change of acidity upon excitation: $\Delta\Delta E_{\text{deprot(enol}-1)} = 0.09$ ev, $\Delta\Delta E_{\text{deprot(keto}-1)} = -0.08$ ev.

3. Keto+1 could be formed from enol0 or keto0 by protonation in the excited state because

the corresponding $\Delta E^*_{\rm prot}$ is markedly larger than $\Delta E_{\rm prot}$ in the corresponding Forster cycle: $\Delta\Delta E_{\rm prot(enol0)} = 0.78$ ev, $\Delta\Delta E_{\rm prot(keto0)} = 0.56$ ev, implying the basicity of 5-C in enol0 or of the 4-carbonyl oxygen in keto0 greatly increases upon electronic excitation.

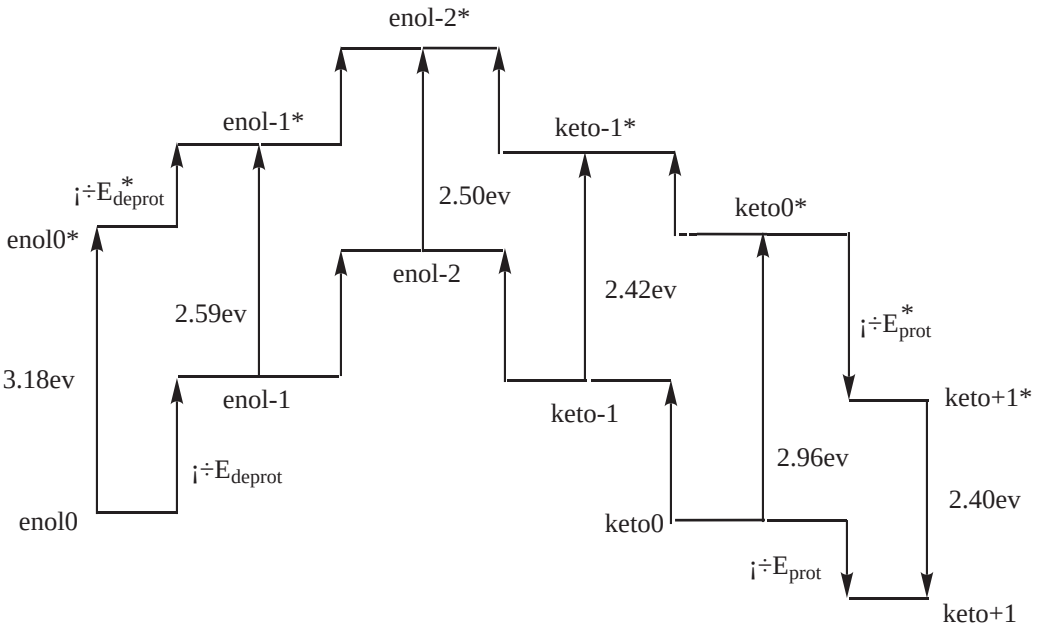

FIG. 5.4: Excitation energies ($S_0 \rightarrow S_1$) of $OxyLH_2$ predicted by TD B3LYP/6-31+G*//B3LYP/6-31+G* in PCM water. These energies are used in the construction of the Forster cycles discussed in the text.

Taking a comprehensive view, it can be deduced that no fluorescence maximum in aqueous solution corresponds to enol-2 as it cannot be formed in either the ground or excited state. The yellow-green fluorescence ($\lambda_{\rm max}$=560 nm) emitter correspondeds to enol-1. The observed single exponential fluorescence decay of $OxyLH_2$ in the yellow-green region in aqueous solution (pH=7.8) supports this conclusion [17]. In addition, at much greater concentration of H^+ (pH<3), the neutral forms (3<pH<8, $\lambda_{\rm max}$=450 nm) could be protonated. Keto+1 is a possible red light emitter ($\lambda_{\rm max}$=620 nm). The present theoretical prediction (606 nm) agrees very well with the earlier experimental result.

Effects of Counterions

In order to mimic the experimental environment in the chemiluminescence experiments which were carried out in DMSO with added potassium *tert*-butoxide [11, 12], Nakatani et al. added K^+ ions to the various anionic forms of $OxyLH_2$ in their calculations and the emission spectra shifted to the blue compared to the computations without the K^+ [24]. To our knowledge, that was the

first attempt to consider the counterions in the computational models of $OxyLH_2$ fluorescence. As NaOH was used to alter the pH in aqueous solution in several experiments [17], the [enol-2]-2Na tight ion pair complex (see Fig. 5.3) was considered to reveal the effects of counterions. The model is somewhat oversimplified as in the real aqueous solution the Na^+ also would interact explicitly with water molecules.

Inclusion of Na^+ causes a 10∼20 nm blue shift in the emission spectra, λ_{max}, of the anions (Table 5.2). Charge distribution analysis in the exited state shows Na^+ is well formed in PCM water. In order to ensure that this blue shift effect is due to the Na^+ but the geometric changes, Na was deleted from the optimized geometries of the complexes and emission energies were calculated. Virtually no differences are seen (compare the first and third sets of data in Table 5.2).

Table 5.2: Emission spectra, λ_{max}, in nm, and oscillator strengths, f, predicted for anionic $OxyLH_2$ and the complexes with Na by TD B3LYP/6-31+G*//CIS/6-31G* in PCM water.

	anion		Na added		Na deleted[a]	
	λ_{max}	f	λ_{max}	f	λ_{max}	f
enol-1	507	0.80	499	0.80	506	0.81
keto-1	509	0.78	500	0.77	506	0.79
enol-2	555	0.52	544	0.63	552	0.61

[a] Na deleted: energies calculated at geometries without Na, which were simply deleted from the previously optimized complexes geometries with Na.

Table 5.3: Kohn-Sham Frontier orbital eigenvalues, in eV, predicted for anionic $OxyLH_2$ and the complexes with Na by B3LYP/6-31+G* in PCM water. Energy gaps between HOMO and LUMO are reported.

	anion			Na added			Na deleted		
	HOMO	LUMO	ΔE	HOMO	LUMO	ΔE	HOMO	LUMO	ΔE
enol-1	-4.65	-2.09	2.56	-4.77	-2.17	2.60	-4.66	-2.10	2.56
keto-1	-5.19	-2.70	2.49	-5.32	-2.77	2.55	-5.18	-2.68	2.50
enol-2	-3.61	-1.26	2.35	-4.40	-1.95	2.45	-4.20	-1.77	2.43

How does the Na^+ affect the spectra? Taking enol-2 and its Na-complex for example, their Kohn-Sham (KS) frontier orbitals, HOMO and LUMO, are shown in Fig. 5.5. Clearly the HOMO and LUMO have very similar characteristics with or without the Na, *viz.*, there is no orbital contribution from the Na. Thus, Na^+ affects the emission energies neither by sharing the negative charge of enol-2 nor by significantly changing the forms of the HOMO and LUMO. However, the Na^+ does change the KS eigenvalues of enol-2, which makes the energy gap to be larger. The $\Delta E_{LUMO-HOMO}$ of

enol-2 is 2.35 eV, and with Na^+ included the gap is 2.45 eV. The KS frontier orbital eigenvalues of enol-1, keto-1, and enol-2 are given in Table 5.3. Na^+ stabilizes the HOMO, and as a result the spectra shift a little to the blue. Accordingly, the blue shift of keto-1 chemiluminescence, which occurs on going from water/imidazole to DMSO/potassium *tert*-butoxide [9,11], may due to the K^+ counterions in DMSO.

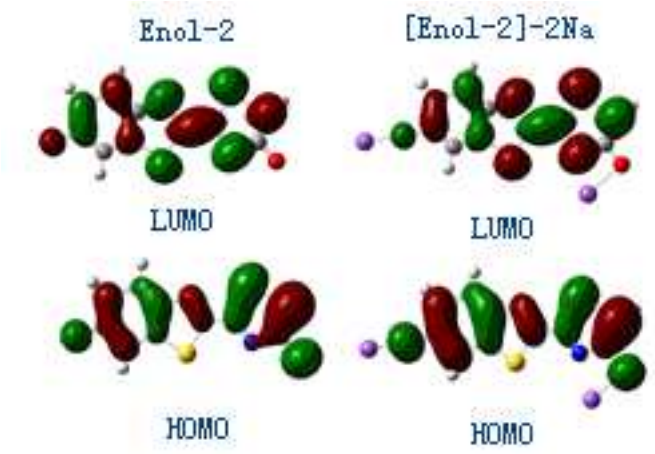

FIG. 5.5: Kohn-Sham frontier orbitals for enol-2 and the [enol-2]-2Na complex predicted with the B3LYP/6-31+G* method in PCM water.

B4. Conclusions

In this study, the mechanism for the fluorescence color tuning of firefly oxyluciferin in aqueous solution was expounded with the use of the TDDFT B3LYP/6-31+G* model. From the predicted emission spectra of various isomers and tautomers of $OxyLH_2$, they are shown to be good emitters in the visible light region. Each species cannot be considered as a fluorescent emitter solely due to agreement between the predicted emission energy and experiment. Keto-1, for example, which was thought to produce the red fluorescence, has no corresponding fluorescence peak in aqueous solution. However, it is still a candidate as the red light emitter in chemi- and bioluminescence for different reaction conditions from those discussed.

In the excited state, neutral $OxyLH_2$ more easily loses its 6′-H proton or gains a proton at 5-C or 4-O. Excited state intramolecular proton transfer may occur. Counterions, such as Na^+ and K^+, cause the emission wavelength of anionic $OxyLH_2$ to shift a little to the blue. Charge transfer within $OxyLH_2$ is insignificant in the planar forms, and the efficient TDDFT approach proved powerful in studying the series of $OxyLH_2$ molecules.

This report has focused on fluorescence in aqueous solution, which must be differentiated from chemi- or bioluminescence.

Reference

[1] B. R. Branchini, M. H. Murtiashaw, R. A. Magyar, N. C. Portier, M. C. Ruggiero, and J. G. Stroh, J. Am. Chem. Soc. 124 (2002) 2112.

[2] T. Nakatsu, S. Ichiyama, J. Hiratake, A. Saldanha, N. Kobashi, K. Sakata, and H. Kato, Nature 440 (2006) 7082.

[3] V. R. Viviani, Cell. Mol. Life. Sci. 59 (2002) 1833.

[4] T. N. Vlasova, O. V. Leontieva, and N. N. Ugarova, Biolumin. Chemilumin.: Prog. Perspect. (2005) 69-72.

[5] B. R. Branchini, T. L. Southworth, M. H. Murtiashaw, R. A. Magyar, S. A. Gonzalez, M. C. Ruggiero, and J. G. Stroh, Biochem. 43 (2004) 7255.

[6] B. R. Branchini, R. A. Magyar, M. H. Murtiashaw, S. M. Anderson, L. C. Helgerson, and M. Zimmer, Biochem. 38 (1999) 13223.

[7] M. Matsumoto, J. Photochem. Photobiol. C, 5 (2004) 27.

[8] G. Orlova, J. D. Goddard, and L. Yu. Brovko, J. Am. Chem. Soc. 125 (2003) 6962.

[9] E. H. White, E. Rapaport, H. H. Seliger, and T. A. Hopkins, Bioorg. Chem. 1 (1971) 92.

[10] H. Fraga, D. Fernandes, J. Novotny, R. Fontes, and J. C. G. Esteves da Silva, ChemBioChem. 7 (2006) 929.

[11] T. A. Hopkins, H. H. Seliger, and E. H. White, J. Am. Chem. Soc. 89 (1967) 7148.

[12] E. H. White, E. Rapaport, T. A. Hopkins, and H. H. Seliger, J. Am. Chem. Soc. 91 (1969) 2178.

[13] E. H. White, M. G. Steinmetz, J. D. Miano, P. D. Wildes, and R. Morland, J. Am. Chem. Soc. 102 (1980) 3199.

[14] W. C. Rhodes, and W. D. McElroy, J. Biol. Chem. 233 (1958) 1528.

[15] O. V. Leontieva, T. N. Vlasova, and N. N. Ugarova, Biochem. (Moscow) 71 (2006) 51.

[16] R. A. Morton, T. A. Hopkins, and H. H. Seliger, Biochem. 8 (1969) 1598.

[17] O. A. Gandelmann, L. Yu. Brovko, N. N. Ugarova, A. Yu. Chikishevb, and A. P. Shkurimov, J. Photochem. Photobiol: B. 19 (1993) 187.

[18] N. Wada, and R. Shibata, J. Phys. Soc. Jap. 66 (1997) 3312.

[19] H. Suzuki, and T. Goto, Agric. Biol. Chem. 36 (1972) 2213.

[20] N. Suzuki, M. Sato, R. Okada, and T. Goto, Tetrahedron 28 (1972) 4065.

[21] A. M. Ren, and J. D. Goddard, J. Photochem. Photobiol: B. 81 (2005) 163.

[22] A. M. Ren, J. F. Guo, J. K. Feng, L. Y. Zou, Z. W. Li, and J. D. Goddard, Chin. J. Chem. 26 (2008) 55.

[23] N. N. Ugarova, L. G. Maloshenok, and I. V. Uporov, Biochem. (Moscow) 70 (2005) 1262.

[24] N. Nakatani, J. Hasegawa, and H. Nakatsuji, J. Am. Chem. Soc. 129 (2007) 8756.

[25] T. Yang, and J. D. Goddard, J. Phys. Chem. A. 111 (2007) 4489.

[26] Y. Ando, K. Niwa, K. Yamada, T. Enomoto, T. Irie, H. Kubota, Y. Ohmiya, and H. Akiyama, Nat. Photonics 2 (2008) 44.

[27] J. Catalan, J. Am. Chem. Soc. 123 (2001) 11940.

[28] K. Fujimoto, S. Hayashi, J. Hasegawa, and H. Nakatsuji, J. Chem. Theory. Comput. 3 (2007) 605.

[29] M. Wanko, M. Hoffmann, P. Strodel, A. Koslowski, W. Thiel, F. Neese, T. Frauenheim, and M. Elstner, J. Phys. Chem. B 109 (2005) 3606.

[30] V. R. Viviani, T. L. Oehlmeyer, F. G. C. Arnoldi, and M. R. Brochetto-Braga, Photochem. Photobiol. 81 (2005) 843.

[31] A. Kitayama, H. Yoshizaki, Y. Ohmiya, H. Ueda, and T. Nagamune, Photochem. Photobiol. 77 (2003) 333.

[32] V. Viviani, A. Uchida, N. Suenaga, M. Ryufuku, and Y. Ohmiya, Biochem. Biophys. Res. Commun. 280 (2001) 1286.

[33] V. R. Viviani, F. G. C. Arnoldi, A. J. S. Neto, T. L. Oehlmeyer, E. J. H. Bechara, and Y. Ohmiya, Photochem. Photobiol. Sci. 2 (2008) 159

[34] A. D. Becke, J. Chem. Phys. 98 (1993) 5648.

[35] M. J. Frisch, G. W. Trucks, H. B. Schlegel, G. E. Scuseria, M. A. Robb, J. R. Cheeseman, J. A. Montgomery Jr., T. Vreven, K. N. Kudin, J. C. Burant, J. M. Millam, S. S. Iyengar, J. Tomasi, V. Barone, B. Mennucci, M. Cossi, G. Scalmani, N. Rega, G. A. Petersson, H. Nakatsuji, M. Hada, M. Ehara, K. Toyota, R. Fukuda, J. Hasegawa, M. Ishida, T. Nakajima, Y. Honda, O. Kitao, H. Nakai, M. Klene, X. Li, J. E. Knox, H. P. Hratchian, J. B. Cross, C. Adamo, J.

Jaramillo, R. Gomperts, R. E. Stratmann, O. Yazyev, A. J. Austin, R. Cammi, C. Pomelli, J. W. Ochterski, P. Y. Ayala, K. Morokuma, G. A. Voth, P. Salvador, J. J. Dannenberg, V. G. Zakrzewski, S. Dapprich, A. D. Daniels, M. C. Strain, O. Farkas, D. K. Malick, A. D. Rabuck, K. Raghavachari, J. B. Foresman, J. V. Ortiz, Q. Cui, A. G. Baboul, S. Clifford, J. Cioslowski, B. B. Stefanov, G. Liu, A. Liashenko, P. Piskorz, I. Komaromi, R. L. Martin, D. J. Fox, T. Keith, M. A. Al-Laham, C. Y. Peng, A. Nanayakkara, M. Challacombe, P. M. W. Gill, B. Johnson, W. Chen, M. W. Wong, C. Gonzalez, and J. A. Pople, GAUSSIAN-03, Revision A.1, (2003) Gaussian, Inc., Pittsburgh, PA.

[36] R. Ahlrichs, M. H. Bar, P. Baron, R. Bauernschmitt, S. Bocker, P. Deglmann, M. Ehrig, K. Eichkorn, S. Elliott, F. Furche, F. Haase, M. Haser, H. Horn, C. Hattig, C. Huber, U. Huniar, M. Kattannek, A. Kohn, C. Kolmel, M. Kollwitz, K. May, C. Ochsenfeld, H. Ohm, H. Patzelt, O. Rubner, A. Schafer, U. Schneider, M. Sierka, O. Treutler, B. Unterreiner, M. V. Arnim, F. Weigend, P. Weis, and H. Weiss, TURBOMOLE-V5-7-patches, Copyright (C) (2004) University of Karlsruhe.

[37] T. Mineva, and N. Russo, Int. J. Quantum Chem. 61 (1997) 665.

[38] H. Houjou, Y. Inoue, and M. Sakurai, J. Am. Chem. Soc. 120 (1998) 4459.

[39] F. Eckert, and A. Klant, AIChE J. 48 (2002) 369.

[40] C. Van Caillie, R. D. Amos, Chem. Phys. Lett. 317 (2000) 159.

[41] J. Jung, C. A. Chin, P. S. Song, J. Am. Chem. Soc. 98 (1976) 3949.

List of Publications

[1] Zhong-wei Li, Ai-min Ren, Jing-fu Guo, Tianxiao Yang, John D. Goddard, and Ji-kang Feng, J. Phys. Chem. A 112 (2008) 9796-9800.

"Color-tuning mechanism in firefly luminescence: theoretical studies on fluorescence of oxyluciferin in aqueous solution using time dependent density functional theory "

[2] Zhong-wei Li, Chun-gang Min, Ai-min Ren, Jing-fu Guo, John D. Goddard, Ji-kang Feng, and Liang Zuo, Bull. Korean Chem. Soc. 31 (2010) 895-900.

"Theoretical study of the relationships between excited state geometry changes and emission energies of oxyluciferin "

[3] Zhong-wei Li, Takehiro Yonehara, and Kazuo Takatsuka, Chem. Phys. 464 (2016) 14-25.

"Nonadiabatic electron wavepacket study on symmetry breaking dynamics of the low-lying excited states of cyclic-B_4 "

Ackownledgement

This thesis is the result of six years study since 2009 at the Graduate School of Arts and Science, University of Tokyo. It represents not only the work I typed before a computer; it is a record of the experiences I have encountered from many unforgettable persons who I wish to acknowledge.

First and foremost, I wish to thank my advisor, Prof. Kazuo Takatsuka, who has been supportive since I first came to Komaba as a foreign student. Especially after my returning to China in 2013, the discussion between us had to be carried out by internet. He guided me academically and emotionally over these years with unbelievable patience. During the most difficult times of life when studied abroad, he gave me shelter as a spiritual pillar.

I also wish to thank our Assistant Prof. Dr. Satoshi Takahashi who takes care of group's affairs meticulously and responsibly besides his own research work. Though we focus on different areas of research, as a faculty, he has been concerned about my growth continuously and more than once helped me out of trouble at the crucial moment.

Thanks also to my seniors in the group. Thanks to Dr. Takehiro Yonehara who has ever spared no effort to help me promote the research process. The most of my study notes just come from his careful instruction. Thanks to Dr. Kengo Nagashima for sharing the valuable experiences in implementing the complex algorithms even at his busiest moments. Without his help, I would have taken much more time for the key programming step. Special thanks to my tutor Dr. Kota Hanasaki, who devotes himself to hard work all the time. No matter how late the evening or how early the morning, his desk lamp at the office was lighted, what was as a lighthouse to me.

Thanks also to Dr. Manabu Kanno, Dr. Yasuki Arasaki, Mrs. Yukiko Kousaka, Dr. Michihiro Okuyama, Dr. Kentaro Yamamoto, Dr. Shin-ichi Koda, and everyone I met at Takatsuka group for continued support and friendship. It is a great pleasure to have met with you! And thanks Japanese goverment MEXT scholarship for financial support.

Special acknowledgements go to the faculty at the Graduate School of Arts and Science. I remember I used to answer a friend in China about something like, "Can you imagine how difficult to educate a Ph. D student? They guided me using their lives."

Lastly, please allow me to thank my parents, whom I thought ordinary persons, yet have ever borne and loved me quietly by their own ways.